

Persistence-Based Statistics for Detecting Structural Changes in High-Dimensional Point Clouds

Toshiyuki Nakayama^{1*}

¹Faculty of Information Science, Shunan University, 843-4-2, Gakuendai, Shunan City, Yamaguchi, 745-8566, Japan.

Corresponding author(s). E-mail(s): nakayama_t25@shunan-u.ac.jp;

Abstract

We study the probabilistic behavior of persistence-based statistics and propose a novel nonparametric framework for detecting structural changes in high-dimensional random point clouds. We establish moment bounds and tightness results for classical persistence statistics—total and maximum persistence—under general distributions, with explicit variance-scaling behavior derived for Gaussian mixture models. Building on these results, we introduce a bounded and normalized statistic based on persistence landscapes combined with the Jensen–Shannon divergence, and we prove its Hölder continuity with respect to perturbations of the input point clouds. The resulting measure is stable, scale- and shift-invariant, and well suited for finite-sample nonparametric inference via permutation testing. An illustrative numerical study using dynamic attribute vectors from decentralized governance data demonstrates the practical applicability of the proposed method. Overall, this work provides a statistically rigorous and computationally stable approach to change-point detection in complex, high-dimensional data.

Keywords: Nonparametric inference, Change-point detection, Random point clouds, Topological data analysis, Persistent homology, Persistence landscapes

1 Introduction

Statistical detection of structural changes in high-dimensional data is a fundamental problem in modern data analysis, with applications ranging from complex networks to

time-evolving multivariate systems. When data are represented as point clouds, such changes often manifest as alterations in their geometric or topological organization. Designing nonparametric and computationally stable procedures that can capture such changes in a distribution-free manner remains a challenging task.

Topological data analysis (TDA) provides a powerful framework for quantifying geometric and topological structure in point cloud data. In many real-world systems, however, the underlying data-generating process evolves over time, leading to gradual or abrupt changes in the associated topology. Understanding how persistence statistics behave under such variability—and how they can be used for statistically rigorous inference—remains an open problem at the interface of statistics, probability theory, and computational topology.

The present work addresses this problem from a theoretical standpoint. We investigate the probabilistic properties of persistence statistics, establish explicit moment bounds and scaling relations under general and Gaussian-mixture settings, and develop a new persistence-based divergence for change detection. Specifically, our contributions are threefold:

- (1) **Moment and tightness results for random persistence:** We derive upper bounds for the p -th moments of total and maximum persistence under minimal distributional assumptions, and we show tightness of the normalized statistics under variance scaling. These results provide new quantitative insight into the stochastic behavior of persistence features.
- (2) **A new persistence-landscape-based divergence:** We define a scale- and shift-invariant statistic combining persistence landscapes with the Jensen–Shannon distance, and we prove its Hölder continuity with respect to perturbations of point clouds. This yields a stable metric suitable for nonparametric statistical inference.
- (3) **Illustrative application to dynamic point clouds:** We demonstrate the proposed framework on time-evolving high-dimensional attribute vectors, detecting regime shifts in a decentralized voting dataset. The example highlights how theoretical stability results translate into practical robustness.

Our study thus contributes to the ongoing effort to build a probabilistic theory of persistent homology, linking classical stochastic analysis with modern TDA. Beyond the illustrative example, the proposed framework applies generally to random point clouds and dynamic metric spaces, providing a mathematically grounded approach to topological change detection.

2 Background and Related Work

2.1 High-Dimensional and Dynamic Point Clouds

Modern data often arise as collections of high-dimensional points whose underlying geometry and topology evolve over time. Examples include dynamic networks, evolving manifolds, and temporal collections of attribute vectors in complex systems. Analyzing such data requires statistical methods that are sensitive to nonlinear structural changes

yet robust to noise and scale variation. A central challenge is to detect significant shifts in the topological organization of these point clouds—that is, changes in their connectivity or higher-dimensional features—without imposing strong distributional assumptions.

Our motivation stems from the general problem of monitoring *random point clouds* generated by stochastic processes whose dispersion or correlation structure may vary over time. While specific applications may include social, biological, or economic systems, the focus of this study is on the mathematical and statistical foundations that enable such topological monitoring in a general probabilistic setting.

2.2 Topological Data Analysis and Related Work

Topological data analysis (TDA) provides a powerful framework for extracting geometric and topological information from point clouds. Through a family of simplicial complexes constructed across varying proximity thresholds—a process known as *filtration*—TDA records the birth and death of topological features in a *persistence diagram*, a multiset of intervals representing the data’s shape. The theoretical foundations of persistent homology were established by [Carlsson \(2009\)](#) and [Edelsbrunner and Harer \(2010\)](#), and have since found numerous applications in the sciences [Lum et al. \(2013\)](#); [Ghrist \(2008\)](#).

To enable statistical analysis, several stable vectorizations of persistence diagrams have been proposed. The *persistence landscape* introduced by [Bubenik \(2015\)](#) represents a diagram as a collection of functions, while the *persistence image* introduced by [Adams et al. \(2017\)](#) provides a smooth, fixed-length embedding. These representations form the basis of the emerging field of *statistical TDA*, which connects persistent homology with classical inference and probability theory.

Recent studies have explored persistence-based indicators of change or instability in complex systems. For instance, [Gidea and Katz \(2018\)](#) applied persistent homology to dynamic correlation networks, while [Islambekov et al. \(2019\)](#) combined persistence features with nonparametric change-point algorithms for environmental data. More recently, [Yao et al. \(2025\)](#) analyzed time-varying financial networks through persistent homology to detect regime shifts. These works highlight the potential of topological methods for detecting structural transitions, yet a unified *theoretical* and *nonparametric* framework for this purpose has not been established.

From a statistical perspective, many existing persistence-based approaches focus primarily on feature extraction or empirical summaries, while questions of finite-sample behavior, distribution-free inference, and computational stability under data perturbations remain comparatively less explored.

The present study addresses this gap by developing a mathematically grounded, persistence-based framework for detecting structural changes in random point clouds. We establish moment and tightness bounds for classical persistence statistics and prove stability and continuity results for a newly defined landscape-based divergence.

3 Persistence Statistics and Moment Bounds

This section adopts a standard formal framework for the persistent homology of finite point clouds, where persistence diagrams are treated as diagram-valued mappings induced from the data through filtration constructions. The overall setup—including the representation of a point cloud as a finite subset of a metric space and the use of persistence-based real-valued quantities derived from filtrations—follows the general formulation introduced by [Carrière et al. \(2021\)](#). Within this framework, we focus on probabilistic moment bounds and scaling properties of persistence statistics.

3.1 Persistence Statistics

Let $d, N \in \mathbb{N}$ and let $x = (x_1, \dots, x_N) \in \mathcal{X}^N$ be a finite point cloud in $\mathcal{X} := \mathbb{R}^d$, where each element of \mathcal{X} represents an attribute vector. The set of all filtrations on the full simplex $K = 2^{\{1, \dots, N\}} \setminus \{\emptyset\}$ is

$$\text{Filt}_K = \left\{ \Phi = (\Phi_\sigma)_{\sigma \in K} \in \mathbb{R}^{|K|} : \sigma_1 \subset \sigma_2 \implies \Phi_{\sigma_1} \leq \Phi_{\sigma_2} \right\} \subset \mathbb{R}^{2^N - 1}.$$

Here, $|K|$ denotes the cardinality of K .

Let Dgm denote the space of persistence diagrams, i.e. locally finite multisets on $\{(b, d) \in \overline{\mathbb{R}}^2 : b < d\}$ with the convention that the diagonal $\{(t, t) : t \in \overline{\mathbb{R}}\}$ has infinite multiplicity. We endow Dgm with the bottleneck distance d_B (Appendix A.4). The map

$$\text{Pers}_\ell : \text{Filt}_K \rightarrow \text{Dgm}$$

assigns to each filtration its persistence diagram in homological degree $\ell \in \mathbb{N}_0$; this is the *persistence map*. (Basic notions of simplicial complexes, homology, and persistence diagrams are recalled in Appendix A.)

For any $D \in \text{Dgm}$, define the *total persistence* in degree $\ell \in \mathbb{N}_0$ $E_{\ell, \text{total}} : \text{Dgm} \rightarrow \mathbb{R}$ by

$$E_{\ell, \text{total}}(D) = \sum_{(b, d) \in D, d < \infty} (d - b),$$

where the sum is taken with multiplicities. Similarly, for any $D \in \text{Dgm}$, define the *maximum persistence* in degree $\ell \in \mathbb{N}_0$ $E_{\ell, \text{max}} : \text{Dgm} \rightarrow \mathbb{R}$ by

$$E_{\ell, \text{max}}(D) = \max_{(b, d) \in D, d < \infty} (d - b).$$

Both quantities are finite for finite diagrams, and intuitively measure the total and maximal lifespans of ℓ -dimensional topological features.

Vietoris–Rips filtration.

In what follows we work with the Vietoris–Rips filtration map $\Phi : \mathcal{X}^N \rightarrow \text{Filt}_K$, defined by

$$\Phi_\sigma(x) := \max_{i, j \in \sigma} \|x_i - x_j\|, \quad \sigma \in K, \tag{1}$$

where $\|\cdot\|$ denotes the Euclidean norm. This yields the *Vietoris–Rips persistence diagram map* $\mathcal{D}_\ell: \mathcal{X}^N \rightarrow \text{Dgm}$ in degree ℓ , defined by

$$\mathcal{D}_\ell(x) := \text{Pers}_\ell(\Phi(x)) \in \text{Dgm}, \quad x \in \mathcal{X}^N.$$

Remark 1 Here we adopt the convention that the Vietoris–Rips filtration parameter is given by the pairwise distance itself, rather than by half the distance. This choice is consistent with standard implementations such as Gudhi.

Example 1 (Three-point configuration) Let $x = (x_1, x_2, x_3) \in (\mathbb{R}^d)^3 = \mathcal{X}^3$, and let $s_{(1)}(x) \leq s_{(2)}(x) \leq s_{(3)}(x)$ be the ordered pairwise distances $\{\|x_1 - x_2\|, \|x_1 - x_3\|, \|x_2 - x_3\|\}$. The Vietoris–Rips filtration values are

$$\begin{aligned} \Phi_{\{i\}}(x) &= 0 \quad (i = 1, 2, 3), \\ \Phi_{\{i,j\}}(x) &= \|x_i - x_j\| \quad (1 \leq i < j \leq 3), \\ \Phi_{\{1,2,3\}}(x) &= s_{(3)}(x). \end{aligned}$$

The resulting diagrams are given by

$$\begin{aligned} \mathcal{D}_0(x) &= \{(0, s_{(1)}(x))\} \uplus \{(0, s_{(2)}(x))\} \uplus \{(0, \infty)\}, \\ \mathcal{D}_\ell(x) &= \emptyset, \quad \ell \geq 1. \end{aligned}$$

Here, the symbol \uplus denotes the disjoint union of finite multisets, so that multiplicities of identical birth–death pairs are added accordingly. These represent the creation and merging of connected components in H_0 . Hence

$$E_{0,\text{total}}(\mathcal{D}_0(x)) = s_{(1)}(x) + s_{(2)}(x), \quad E_{0,\text{max}}(\mathcal{D}_0(x)) = s_{(2)}(x).$$

3.2 Continuity and Regularity of Persistence Statistics

In what follows, to evaluate quantities such as expectations of powers of persistence statistics (total and maximum persistence) (see Section 3.1), we first confirm basic regularity (continuity and semicontinuity, hence measurability):

Proposition 1 (Basic Regularity) *Under the setting of Section 3.1, the following follows.*

- (i) *For each ℓ , map $\text{Pers}_\ell: \text{Filt}_K \rightarrow \text{Dgm}$ is continuous (with respect to d_B).*
- (ii) *For each ℓ , map $\mathcal{D}_\ell = \text{Pers}_\ell \circ \Phi: \mathcal{X}^N \rightarrow \text{Dgm}$ is continuous.*
- (iii) *For each ℓ , map $E_{\ell,\text{max}}: \text{Dgm} \rightarrow \mathbb{R}$ is continuous and $E_{\ell,\text{total}}: \text{Dgm} \rightarrow \mathbb{R}$ is lower semicontinuous.*

Proof (i) The continuity of each Pers_ℓ follows from the stability of persistence diagrams with respect to the bottleneck distance, as shown by Cohen-Steiner et al. (2007).

(ii) The filtration map $\Phi: \mathcal{X}^N \rightarrow \text{Filt}_K$ in (1) is continuous (it is a composition of continuous maps of Euclidean distances). Thus $\mathcal{D}_\ell = \text{Pers}_\ell \circ \Phi$ is continuous as a composition of continuous maps.

(iii) This is already known; see, e.g., Cohen-Steiner et al. (2007). □

We may now define the following maps:

$$\begin{aligned}\mathcal{L}_{\ell,\text{total}} &:= E_{\ell,\text{total}} \circ \mathcal{D}_{\ell} : \mathcal{X}^N \rightarrow \mathbb{R}, \\ \mathcal{L}_{\ell,\text{max}} &:= E_{\ell,\text{max}} \circ \mathcal{D}_{\ell} : \mathcal{X}^N \rightarrow \mathbb{R}.\end{aligned}$$

These maps assign to each point cloud the total or maximum bar length of its persistence diagram. By Proposition 1, they are at least lower semicontinuous and hence measurable. In the next section, we endow the point cloud with a probability distribution and evaluate the p -th moments of these maps.

3.3 Moment Bounds for General Distributions

Let $(\Omega, \mathcal{F}, \mathbb{P})$ be a probability space. We define the random vector

$$X = (X_1, \dots, X_N) : \Omega \rightarrow \mathcal{X}^N,$$

where X_1, \dots, X_N are \mathcal{X} -valued random variables having the same marginal distribution under \mathbb{P} , but not necessarily independent. (Here, each $X_i \in \mathcal{X}$ represents one attribute vector.) Throughout, $\mathbb{E}[\cdot]$ denotes the expectation with respect to \mathbb{P} .

Throughout this section, let $\ell \in \mathbb{N}_0$ be arbitrary and set

$$\mathcal{L}_{\ell} := \{\mathcal{L}_{\ell,\text{total}}, \mathcal{L}_{\ell,\text{max}}\}.$$

We write $\mathcal{L} \in \mathcal{L}_{\ell}$ for a generic element of this set. We first provide an upper bound on the p -th moment of $\mathcal{L}(X)$ without assuming any specific distribution for X .

Theorem 2 (Moment Bounds of Persistence Statistics for General Distributions) *For any $p \geq 1$, the following inequality holds:*

$$\mathbb{E} [\mathcal{L}(X)^p] \leq C_{\ell,p}^{\text{VR}}(N) \mathbb{E} [\|X_1\|^p],$$

where $\|\cdot\|$ is the Euclidean norm and

$$n_{\ell}(N) := \min \left\{ \binom{N}{\ell+1}, \binom{N}{\ell+2} \right\}, \quad C_{\ell,p}^{\text{VR}}(N) := 2^p N (n_{\ell}(N))^p.$$

Proof Since

$$\mathcal{L}_{\ell,\text{max}}(x) \leq \mathcal{L}_{\ell,\text{total}}(x), \quad x \in \mathcal{X}^N,$$

it suffices to prove the theorem for $\mathcal{L}_{\ell,\text{total}}$ only.

Each finite bar in degree ℓ corresponds to a unique pairing between an ℓ -simplex and an $(\ell+1)$ -simplex in the standard matrix-reduction algorithm [Edelsbrunner et al. \(2002\)](#); [Edelsbrunner and Harer \(2010\)](#), implying that the number of finite bars is bounded by

$$\#\{\text{finite bars in } H_{\ell}\} \leq n_{\ell}(N).$$

By Hölder's inequality we have

$$\mathbb{E} [\mathcal{L}_{\ell,\text{total}}(X)^p] \leq n_{\ell}(N)^{p-1} I, \tag{2}$$

where we set

$$I := \mathbb{E} \left[\sum_{\substack{(b, d) \in \text{Pers}_\ell(\Phi(X)) \\ d < \infty}} (d - b)^p \right].$$

In the case of Vietoris-Rips filtration, the filtration value of the vertex is 0 (see the definition (1)), so we have

$$\begin{aligned} I &\leq n_\ell(N) \mathbb{E} \left[\max_{\sigma_1, \sigma_2 \in K} |\Phi_{\sigma_1}(X) - \Phi_{\sigma_2}(X)|^p \right] \\ &= n_\ell(N) \mathbb{E} \left[\max_{\sigma \in K} |\Phi_\sigma(X)|^p \right]. \end{aligned}$$

Again, from the definition of the Vietoris-Rips filtration in (1), we obtain

$$\begin{aligned} I &\leq n_\ell(N) \mathbb{E} \left[\max_{j_1, j_2 \in \{1, \dots, N\}} \|X_{j_1} - X_{j_2}\|^p \right] \\ &\leq n_\ell(N) \mathbb{E} \left[\max_{j_1, j_2 \in \{1, \dots, N\}} (\|X_{j_1}\| + \|X_{j_2}\|)^p \right] \\ &\leq 2^p n_\ell(N) \mathbb{E} \left[\max_{j \in \{1, \dots, N\}} \|X_j\|^p \right] \\ &\leq 2^p n_\ell(N) \sum_{j=1}^N \mathbb{E} [\|X_j\|^p] = 2^p N n_\ell(N) \mathbb{E} [\|X_1\|^p]. \end{aligned}$$

Combining the equation (2) leads to the conclusion. \square

3.4 Moment Bounds and Tightness under GMMs

In the previous section, we established Theorem 2, which provides moment bounds for persistence statistics under general distributions. Here we focus on the special case where the data points are drawn from a Gaussian mixture model (GMM).

Remark 2 It is well known that GMMs are universal approximators of probability densities on \mathbb{R}^d . That is, any probability distribution can be approximated arbitrarily well by a finite mixture of Gaussian components (see, e.g., McLachlan and Peel (2000); Li and Barron (2000)). This property justifies the use of GMMs as flexible models for complex data distributions such as attribute vectors.

For integers $d, K \geq 1$, consider a d -dimensional GMM with mixture weights (π_1, \dots, π_K) , mean vectors $\mu_1, \dots, \mu_K \in \mathbb{R}^d$, and covariance matrices $\eta \Sigma_1, \dots, \eta \Sigma_K$, where $\eta > 0$ is a common variance-scaling factor and $\Sigma_1, \dots, \Sigma_K \in \mathbb{S}_+^d$ are the unscaled covariances. Here

$$\mathbb{S}_+^d := \{A \in \mathbb{R}^{d \times d} : A = A^\top, A \succeq 0\}$$

denotes the cone of symmetric positive semidefinite (PSD) matrices. We use the Loewner order: $A \succeq B$ means $A - B$ is PSD, and $A \succ 0$ denotes positive definite (PD). Allowing $\Sigma_k \succeq 0$ permits singular covariances. Let P_η denote the corresponding probability distribution on $\mathcal{X} = \mathbb{R}^d$.

Let $(\Omega, \mathcal{F}, \mathbb{P})$ be a probability space. On this probability space, we define the random vector

$$X^{(\eta)} = (X_1^{(\eta)}, \dots, X_N^{(\eta)}) : \Omega \rightarrow \mathcal{X}^N,$$

where $X_1^{(\eta)}, \dots, X_N^{(\eta)}$ are \mathcal{X} -valued random variables sharing the same marginal distribution P_η ; they are not required to be independent unless stated otherwise.

Throughout, we use the notation $N(\mu_k, \Sigma_k)$ to denote the Gaussian law with mean μ_k and covariance $\Sigma_k \in \mathbb{S}_+^d$, allowing for singular Σ_k .

Remark 3 (Gaussian distributions with possibly singular covariance matrices) Let

$$\Sigma_k = U \operatorname{diag}(\lambda_1, \dots, \lambda_d) U^\top, \quad U^\top U = I, \quad \lambda_i \geq 0.$$

(Recall that every real symmetric PSD matrix admits such a decomposition, with nonnegative eigenvalues.) The law $N(\mu_k, \Sigma_k)$ can be specified in any of the following equivalent ways:

Principal square root. The matrix Σ_k admits the unique symmetric positive semidefinite square root, called the *principal square root*, denoted by $\Sigma_k^{1/2}$, and given by

$$\Sigma_k^{1/2} = U \operatorname{diag}(\sqrt{\lambda_1}, \dots, \sqrt{\lambda_d}) U^\top.$$

(Although the eigenbasis U need not be unique, the product above is unique.) If $Z_d \sim N(0, I_d)$, then

$$\mu_k + \Sigma_k^{1/2} Z_d \sim N(\mu_k, \Sigma_k) \quad (\operatorname{Cov}(\Sigma_k^{1/2} Z_d) = \Sigma_k^{1/2} (\Sigma_k^{1/2})^\top = \Sigma_k).$$

Thin factor (rank- r_k representation). Let $r_k = \operatorname{rank}(\Sigma_k)$ and collect the eigenvectors corresponding to the *positive* eigenvalues into $U_r = [u_i : \lambda_i > 0] \in \mathbb{R}^{d \times r_k}$, and set $\Lambda_r = \operatorname{diag}(\lambda_i : \lambda_i > 0)$. Define

$$B_k := U_r \Lambda_r^{1/2} \in \mathbb{R}^{d \times r_k}.$$

Then $\Sigma_k = B_k B_k^\top$, and for $Z_{r_k} \sim N(0, I_{r_k})$ we have

$$\mu_k + B_k Z_{r_k} \sim N(\mu_k, \Sigma_k) \quad (\operatorname{Cov}(B_k Z_{r_k}) = B_k B_k^\top = \Sigma_k).$$

Note that B_k is not unique: $B_k Q$ with any orthogonal $Q \in \mathbb{R}^{r_k \times r_k}$ yields the same covariance.

The characteristic function. Use the characteristic function $\exp(it^\top \mu_k - \frac{1}{2} t^\top \Sigma_k t)$ for $t \in \mathbb{R}^d$.

Remark 4 (Key Features of Our Model) For the modeling described above, we note the following points.

- (i) Throughout we work with (possibly singular) symmetric positive semidefinite covariances $\Sigma_k \in \mathbb{S}_+^d$ and do not assume strict positive definiteness. This modeling choice accommodates effectively low-rank components that arise in practice—for instance, in the voting context, this occurs under strong substitutability among candidates, where voters treat groups of candidates as equivalent, causing their allocated scores (ratings) to co-move (e.g., approximately constant-sum) and induce near-linear dependencies. While many software implementations insert a small diagonal loading for numerical stability (e.g., $\Sigma_k \mapsto \Sigma_k + \lambda_0 I_d$ with a small $\lambda_0 > 0$), our results are formulated for $\Sigma_k \succeq 0$ and remain valid in the vanishing regularization limit $\lambda_0 \downarrow 0$.
- (ii) As usual, the mixture is identifiable only up to permutation of component labels; all results below are invariant under such permutations.

(iii) If Σ_k is singular, the k -th Gaussian component $\mathcal{N}(\mu_k, \Sigma_k)$ is supported on the affine subspace $\mu_k + \text{Im}(\Sigma_k)$ (equivalently, $\mu_k + \text{Im}(\Sigma_k^{1/2})$). Therefore

$$\text{supp}(P_\eta) = \overline{\bigcup_{k: \pi_k > 0} (\mu_k + \text{Im}(\Sigma_k))}.$$

In particular, $\text{supp}(P_\eta) = \mathbb{R}^d$ if at least one component has $\Sigma_k \succ 0$.

We introduce a constant that will be used in subsequent estimates.

Definition 1 (Gaussian Moment Constant) Let $p \geq 1$. Define

$$\kappa_{d,p} := \mathbb{E}[\|Z\|^p] = 2^{p/2} \frac{\Gamma\left(\frac{d+p}{2}\right)}{\Gamma\left(\frac{d}{2}\right)},$$

where $Z \sim N(0, I_d)$ and $\|\cdot\|$ is the Euclidean norm.

Remark 5 The closed form in Definition 1 follows from the fact that $\|Z\|$ has the χ_d distribution, i.e., the distribution of the square root of a χ_d^2 random variable. The p -th moment of the χ_d distribution is well known; see, e.g., [Vershynin \(2018, Sec. 2.3\)](#) or [Muirhead \(1982, Ch. 1\)](#), yielding

$$\mathbb{E}[\|Z\|^p] = 2^{p/2} \frac{\Gamma\left(\frac{d+p}{2}\right)}{\Gamma\left(\frac{d}{2}\right)}.$$

Using this constant, we can bound the p -th moments of general Gaussian vectors as follows.

Lemma 3 (Moment Bound for Gaussian Vectors) *Let $p \geq 1$ and let $\mu \in \mathbb{R}^d, \Sigma \in \mathbb{S}_+^d$. If $Y \sim N(\mu, \Sigma)$, then*

$$\mathbb{E}[\|Y\|^p] \leq 2^{p-1} \left\{ \|\mu\|^p + \kappa_{d,p} (\text{tr } \Sigma)^{p/2} \right\}.$$

Proof Let $Z \sim N(0, I_d)$ and write $Y = \mu + \Sigma^{1/2}Z$, where $\Sigma^{1/2}$ is the principal square root defined in Remark 3. Then we have

$$\begin{aligned} \|Y\| &\leq \|\mu\| + \|\Sigma^{1/2}Z\| \\ &\leq \|\mu\| + \|\Sigma^{1/2}\|_{\text{F}} \|Z\| = \|\mu\| + (\text{tr } \Sigma)^{1/2} \|Z\|, \end{aligned}$$

where $\|\cdot\|_{\text{F}}$ is the Frobenius norm on matrices, defined by $\|A\|_{\text{F}} := \sqrt{\text{tr}(A^\top A)}$.

From Hölder's inequality, we have

$$\begin{aligned} \mathbb{E}[\|Y\|^p] &\leq 2^{p-1} \left(\|\mu\|^p + (\text{tr } \Sigma)^{p/2} \mathbb{E}[\|Z\|^p] \right) \\ &= 2^{p-1} \left\{ \|\mu\|^p + \kappa_{d,p} (\text{tr } \Sigma)^{p/2} \right\}. \end{aligned}$$

□

Lemma 4 (Norm Estimate for a Point in the Point Cloud) *For any $p \geq 1$, there exist constants $M_p, V_p > 0$ such that*

$$\mathbb{E} \left[\|X_j^{(\eta)}\|^p \right] \leq M_p + V_p \eta^{p/2}, \quad j = 1, \dots, N, \quad \eta > 0.$$

Here we can choose as follows:

$$M_p = 2^{p-1} \sum_{k=1}^K \pi_k \|\mu_k\|^p, \quad V_p = 2^{p-1} \kappa_{d,p} \sum_{k=1}^K \pi_k (\text{tr } \Sigma_k)^{p/2}.$$

Proof From Lemma 3, we have

$$\begin{aligned} \mathbb{E} \left[\|X_j^{(\eta)}\|^p \right] &= \sum_{k=1}^K \pi_k \mathbb{E} \left[\|Y_k^{(\eta)}\|^p \right] \quad (Y_k^{(\eta)} \sim \mathcal{N}(\mu_k, \eta \Sigma_k)) \\ &\leq 2^{p-1} \sum_{k=1}^K \pi_k \left(\|\mu_k\|^p + \kappa_{d,p} (\text{tr } \Sigma_k)^{p/2} \eta^{p/2} \right) = M_p + V_p \eta^{p/2}. \end{aligned}$$

This completes the proof. \square

We now evaluate persistence statistics under variance scaling for GMMs.

Theorem 5 (Moment Bounds of Persistence Statistics for GMMs) *For any $p \geq 1$ and any $\mathcal{L} \in \mathcal{L}_\ell$, there exist constants $C_{\ell,p}^{(0)}(N), C_{\ell,p}^{(1)}(N) > 0$ such that the following inequality holds:*

$$\mathbb{E} \left[\mathcal{L}(X^{(\eta)})^p \right] \leq C_{\ell,p}^{(0)}(N) + C_{\ell,p}^{(1)}(N) \eta^{p/2}, \quad \eta > 0.$$

Here we can choose as follows:

$$C_{\ell,p}^{(0)}(N) = M_p C_{\ell,p}^{\text{VR}}(N), \quad C_{\ell,p}^{(1)}(N) = V_p C_{\ell,p}^{\text{VR}}(N),$$

where $C_{\ell,p}^{\text{VR}}(N)$ is defined in Theorem 2.

In particular, for the same p we have

$$\sup_{\eta \geq 1} \mathbb{E} \left[(\mathcal{L}(X^{(\eta)}) / \sqrt{\eta})^p \right] \leq C_{\ell,p}(N),$$

where we set

$$C_{\ell,p}(N) := C_{\ell,p}^{(0)}(N) + C_{\ell,p}^{(1)}(N).$$

Proof By Theorem 2, $\mathbb{E}[\mathcal{L}(X^{(\eta)})^p] \leq C_{\ell,p}^{\text{VR}}(N) \mathbb{E}[\|X_1^{(\eta)}\|^p]$. Lemma 4 yields $\mathbb{E}[\|X_1^{(\eta)}\|^p] \leq M_p + V_p \eta^{p/2}$. Combine them and set $C_{\ell,p}^{(0)}(N) = M_p C_{\ell,p}^{\text{VR}}(N)$, $C_{\ell,p}^{(1)}(N) = V_p C_{\ell,p}^{\text{VR}}(N)$. The “in particular” part follows by dividing by $\eta^{p/2}$ and taking $\sup_{\eta \geq 1}$. \square

By normalizing persistence statistics by the square root of the variance multiplier, we can ensure that the probability of leaving a certain compact set is sufficiently small, as shown below.

Corollary 6 (Tightness of the Normalized Persistence Statistics) *For any $\mathcal{L} \in \mathcal{L}_\ell$, the family $\{\mathcal{L}(X^{(\eta)})/\sqrt{\eta}\}_{\eta \geq 1}$ is tight on \mathbb{R} . In particular, for any $\varepsilon > 0$ there exists $U_{\varepsilon, \ell, p}(N) > 0$ such that*

$$\sup_{\eta \geq 1} \mathbb{P} \left(\frac{\mathcal{L}(X^{(\eta)})}{\sqrt{\eta}} > U_{\varepsilon, \ell, p}(N) \right) < \varepsilon,$$

where we can choose

$$U_{\varepsilon, \ell, p}(N) := \left(\frac{C_{\ell, p}(N)}{\varepsilon} \right)^{1/p},$$

with $C_{\ell, p}(N)$ defined in Theorem 5.

Proof By Theorem 5, $\sup_{\eta \geq 1} \mathbb{E}[(\mathcal{L}(X^{(\eta)})/\sqrt{\eta})^p] \leq C_{\ell, p}(N) < \infty$ for some $p \geq 1$. Markov's inequality yields $\sup_{\eta \geq 1} \mathbb{P}(\mathcal{L}(X^{(\eta)})/\sqrt{\eta} > U) \leq C_{\ell, p}(N)/U^p$. Choosing $U_{\varepsilon, \ell, p}(N) = (C_{\ell, p}(N)/\varepsilon)^{1/p}$ completes the proof. \square

Since the family is tight, every sequence has a weakly convergent subsequence, as shown below.

Corollary 7 *For any sequence $\{\eta_n\}_{n \geq 1} \subset [1, \infty)$, there exists a subsequence $\{\eta_{n_k}\}_{k \geq 1}$ such that $\mathcal{L}(X^{(\eta_{n_k})})/\sqrt{\eta_{n_k}}$ converges in distribution to some probability measure on \mathbb{R} as $k \rightarrow \infty$.*

Proof By Corollary 6 the family is tight; since \mathbb{R} is Polish, Prokhorov's theorem gives relative compactness in the weak topology. \square

To quantify the scale of the statistic, we prove that the upper tail above a constant multiple of $\sqrt{\eta}$ is uniformly small.

Corollary 8 (Uniform polynomial tail at the $\sqrt{\eta}$ -scale) *Fix $\mathcal{L} \in \mathcal{L}_\ell$ and $p \geq 1$. Let $C_{\ell, p}(N) > 0$ be the constant from Theorem 5. Then for all $t > 0$,*

$$\sup_{\eta \geq 1} \mathbb{P} \left(\frac{\mathcal{L}(X^{(\eta)})}{\sqrt{\eta}} \geq t \right) \leq \frac{C_{\ell, p}(N)}{t^p}.$$

Equivalently,

$$\sup_{\eta \geq 1} \mathbb{P} \left(\mathcal{L}(X^{(\eta)}) \geq t \sqrt{\eta} \right) \leq \frac{C_{\ell, p}(N)}{t^p} \quad (t > 0).$$

In particular, for all ε , taking $t = (C_{\ell, p}(N)/\varepsilon)^{1/p}$ gives

$$\sup_{\eta \geq 1} \mathbb{P} \left(\frac{\mathcal{L}(X^{(\eta)})}{\sqrt{\eta}} \geq (C_{\ell, p}(N)/\varepsilon)^{1/p} \right) \leq \varepsilon.$$

Proof For $\eta \geq 1$,

$$\mathbb{E} \left[\left(\frac{\mathcal{L}(X^{(\eta)})}{\sqrt{\eta}} \right)^p \right] = \frac{\mathbb{E}[\mathcal{L}(X^{(\eta)})^p]}{\eta^{p/2}} \leq \frac{C_{\ell,p}^{(0)}(N) + C_{\ell,p}^{(1)}(N) \eta^{p/2}}{\eta^{p/2}} = C_{\ell,p}(N).$$

Since $\mathcal{L}(X^{(\eta)}) \geq 0$, apply the generalized Markov inequality to $Y_\eta := \mathcal{L}(X^{(\eta)})/\sqrt{\eta}$:

$$\mathbb{P}(Y_\eta \geq t) = \mathbb{P}(Y_\eta^p \geq t^p) \leq \frac{\mathbb{E}[Y_\eta^p]}{t^p} \leq \frac{C_{\ell,p}(N)}{t^p}.$$

Taking the supremum over $\eta \geq 1$ proves the claim. \square

Remark 6 (Role of moment bounds, tightness, and variance scaling) The results of this section serve a conceptual and methodological role that goes beyond the specific Gaussian mixture setting in which they are derived.

(i) **Beyond trivial global rescaling.** While a deterministic rescaling of a point cloud trivially rescales all Vietoris–Rips filtration values, the setting considered in Theorem 5 is fundamentally different. Here, the mean structure of the distribution is fixed, and only the covariance matrices are scaled. Thus, the observed $\sqrt{\eta}$ –growth of persistence statistics reflects increasing *stochastic dispersion* around fixed reference locations, rather than a uniform geometric dilation. This distinction is essential in applications where scale changes arise from heterogeneity or volatility, rather than from a deterministic rescaling of the data.

(ii) **Tightness and uniform tail control.** Corollary 6 and Corollary 8 establish that, after normalization by $\sqrt{\eta}$, classical persistence statistics form a tight family with uniform polynomial tail bounds. These results provide non-asymptotic control over the magnitude and variability of persistence-based quantities under increasing dispersion. In particular, they justify the use of scale-normalized or bounded statistics when comparing random point clouds whose intrinsic variability may differ.

(iii) **Motivation for bounded and normalized statistics.** The variance-scaling behavior quantified in Theorem 5 highlights a limitation of raw persistence summaries: their magnitude is dominated by dispersion effects. This observation motivates the construction in Section 4.1 of the PL+JS statistic, which suppresses scale-driven growth by normalization and regularization, while retaining sensitivity to changes in topological structure. In this sense, the results of this section provide the probabilistic foundation for why a bounded, scale-insensitive comparison of persistence diagrams is desirable for nonparametric inference and change-point detection.

Taken together, the moment bounds, tightness, and uniform tail estimates clarify the stochastic behavior of classical persistence statistics and explain their role as a theoretical benchmark. They do not directly enter the definition of the PL+JS statistic, but they motivate its design and delineate the regime in which purely scale-driven variability should be factored out.

4 A Persistence-Based Statistic for Comparing Random Point Clouds

4.1 Definition of the PL+JS Statistic

We now introduce a scale-bounded, distribution-free statistic for comparing persistence diagrams. The motivation for this construction builds on the results of the preceding sections.

In Sections 3.3 and 3.4, we showed that classical persistence statistics, such as total and maximum persistence, typically increase with the dispersion of the underlying data distribution, and in particular scale with the variance multiplier under Gaussian mixture models. While this behavior is natural from a geometric viewpoint, it implies that raw persistence quantities are inherently sensitive to global scale and may obscure more subtle structural changes.

The PL+JS statistic is designed to mitigate this effect by normalizing persistence landscapes and comparing them through a bounded, information-theoretic divergence on a fixed support. In this way, the resulting statistic suppresses purely scale-driven variation and enables meaningful comparison of topological structure across samples, making it suitable for nonparametric change-point detection. No distributional assumptions (e.g., Gaussian mixtures) are required at this stage; those models were used earlier only to motivate variance-scaling phenomena.

We fix homological degree $\ell \in \mathbb{N}_0$, and we define a statistic for quantitatively comparing two persistence diagrams $D, D' \in \text{Dgm}$ for two data windows \mathcal{W}_1 and \mathcal{W}_2 . The construction is based on the persistence landscape representation (see Appendix A.5) and the Jensen-Shannon distance (see Appendix B) between the associated probability density functions.

Fix $S > 0$ and let $u_S \in \mathcal{P}([0, S])$ denote the uniform density

$$u_S(t) := \frac{1}{S} \mathbf{1}_{[0, S]}(t), \quad (3)$$

where

$$\mathcal{P}([0, S]) := \{p \in L_+^1([0, S]) : \int_0^S p(t) dt = 1\}$$

denotes the set of all probability density functions on $[0, S]$, and $L_+^1([0, S])$ denotes the cone of nonnegative integrable functions on $[0, S]$.

For $\ell \in \mathbb{N}_0$, $M \in \mathbb{N}$, and $D \in \text{Dgm}$, let $\lambda_{\ell, m}(D) : \mathbb{R} \rightarrow [0, \infty)$ ($m = 1, \dots, M$) denote the first M persistence landscape layers (with the convention that $\lambda_{\ell, m}(D) \equiv 0$ if m exceeds the number of bars), and define $\Lambda_\ell^{(M)} : \text{Dgm} \rightarrow L_+^1([0, S])$ by

$$\Lambda_\ell^{(M)}(D)(t) := \sum_{m=1}^M \lambda_{\ell, m}(D)(t), \quad t \in [0, S]. \quad (4)$$

Set

$$A_\ell(D) := \int_0^S \Lambda_\ell^{(M)}(D)(t) dt. \quad (5)$$

Assumption 1 We assume that every diagram $D \in \text{Dgm}$ is supported in $[0, S] \times [0, S]$ (equivalently, $0 \leq b < d \leq S$ for all $(b, d) \in D$).

Under this assumption, for all $t \in [0, S]$ and $D \in \text{Dgm}$,

$$\begin{aligned} 0 \leq \Lambda_\ell^{(M)}(D)(t) &\leq M \min\{t, S-t\} \leq \frac{1}{2} M S, \\ 0 \leq A_\ell(D) &\leq M \int_0^S \min\{t, S-t\} dt = \frac{M S^2}{4} =: A_{\max}. \end{aligned} \tag{6}$$

For $\theta \in (0, 1]$, define the regularized normalization operator $\text{Reg}_\theta: L_+^1([0, S]) \rightarrow \mathcal{P}([0, S])$ by

$$\text{Reg}_\theta(f)(t) := \frac{f(t) + \theta A_{\max} u_S(t)}{\int_0^S f(s) ds + \theta A_{\max}}.$$

For $\gamma \in [0, 1]$ and any $p \in \mathcal{P}([0, S])$, define the γ -mixture operator $\text{Mix}_\gamma: \mathcal{P}([0, S]) \rightarrow \mathcal{P}([0, S])$ by

$$\text{Mix}_\gamma(p) := (1 - \gamma) p + \gamma u_S.$$

Definition 2 Fix $\ell \in \mathbb{N}_0$, $M \in \mathbb{N}$, and $S > 0$. For $\gamma \in [0, 1]$, $\theta \in (0, 1]$, define the PDF associated with D by

$$p_\ell^{(\gamma, \theta)}(D) := \text{Mix}_\gamma(\text{Reg}_\theta(\Lambda_\ell^{(M)}(D))) \in \mathcal{P}([0, S]).$$

Equivalently,

$$\begin{aligned} p_\ell^{(\gamma, \theta)}(D)(t) &= (1 - \gamma) \frac{\Lambda_\ell^{(M)}(D)(t) + \theta A_{\max} u_S(t)}{A_\ell(D) + \theta A_{\max}} + \gamma u_S(t) \\ &= (1 - \gamma) \frac{\Lambda_\ell^{(M)}(D)(t)}{A_\ell(D) + \theta A_{\max}} + \left\{ \gamma + (1 - \gamma) \frac{\theta A_{\max}}{A_\ell(D) + \theta A_{\max}} \right\} u_S(t). \end{aligned}$$

For two persistence diagrams $D, D' \in \text{Dgm}$, we define the *Persistence Landscape + Jensen-Shannon* (PL+JS) statistic as

$$\Delta_\ell(D, D') := d_{\text{JS}}(p_\ell^{(\gamma, \theta)}(D), p_\ell^{(\gamma, \theta)}(D')),$$

where d_{JS} denotes the Jensen-Shannon distance with logarithm base 2 (so that $\Delta_\ell \in [0, 1]$).

Remark 7 (Interpretability, boundedness, and parameter control) The use of the Jensen-Shannon distance in Definition 2 yields a statistic Δ_ℓ that is bounded in $[0, 1]$, providing a scale-free and directly interpretable measure of discrepancy between persistence diagrams. This boundedness is particularly advantageous for finite-sample nonparametric inference, including permutation-based testing, as it prevents a small number of extreme persistence features from dominating the statistic.

The regularization and mixing parameters θ and γ stabilize the normalization of persistence landscapes when the total landscape mass is small. Their influence is explicit and quantitative: as shown in Proposition 10 and Theorem 9, increasing either parameter improves robustness by reducing the Hölder constant, while smaller values enhance sensitivity to topological signal. Thus, (γ, θ) provide principled control of the stability–sensitivity trade-off rather than ad hoc regularization.

Remark 8 (Landscape sums versus silhouettes) Persistence silhouettes aggregate all triangular functions associated with a diagram into a single weighted average, emphasizing

long-lived features through nonlinear persistence weights Chazal et al. (2015). In contrast, the present work employs the unweighted sum of the first M persistence landscape layers, $\Lambda_\ell^{(M)} = \sum_{m=1}^M \lambda_{\ell,m}$.

This choice is motivated by transparency, stability, and practical controllability. The parameter M governs the amount of topological information included in the statistic in a monotone and easily interpretable manner, and the resulting functional inherits a Lipschitz-type stability bound that grows linearly in M .

From a practical perspective, M can be selected in an adaptive manner. One may begin with a small value of M , capturing only the most dominant topological features, and assess whether structural changes are detected. If no significant differences are observed, M can be increased to incorporate finer-scale features. Since increasing M leads to higher computational cost, its choice naturally reflects a trade-off between statistical sensitivity and computational efficiency.

While silhouettes provide an effective low-dimensional summary, the landscape-sum representation retains an explicit hierarchical ordering of dominant features. This hierarchical structure, together with the tunable parameter M , is particularly advantageous for detecting structural changes in a statistically controlled and computationally feasible manner.

Remark 9 (Global cutoff and comparability) Fixing the cutoff S globally ensures that all probability densities associated with persistence diagrams share the same support $[0, S]$. As a result, Jensen–Shannon distances computed across different pairs of diagrams are strictly comparable. In practice, S should be chosen slightly larger than the maximal finite death time expected in the data to avoid truncation effects.

Remark 10 (Limits of signature-based testing) Any test based on a compressed signature of persistence diagrams necessarily identifies distributions only up to the equivalence relation induced by that signature. Distinct persistence diagrams may therefore become indistinguishable after compression; this phenomenon is intrinsic to any signature-based representation and is well illustrated, for example, by the notion of *Euler equivalence* discussed by Dłotko et al. Dłotko et al. (2024) for the Euler characteristic curve.

Accordingly, the PL+JS statistic is not intended as a complete invariant of persistence diagrams, but as a stable and inference-oriented summary. It is designed to provide reliable power against a broad class of structured alternatives while sacrificing sensitivity to fine-scale differences that are often dominated by noise or sampling variability.

4.2 Continuity of the Proposed Change-Point Detection Statistic

In what follows, we reuse the notation introduced in Section 3.1. Let $\mathcal{X} = \mathbb{R}^d$ with $d \in \mathbb{N}$, where each element of \mathcal{X} represents an individual attribute vector. For each $N \in \mathbb{N}$, let

$$\mathcal{D}_\ell^{(N)}: \mathcal{X}^N \rightarrow \text{Dgm}$$

denote the map that assigns to a finite point cloud $x = (x_1, \dots, x_N)$ the persistence diagram in degree $\ell \in \mathbb{N}_0$ associated with the Vietoris–Rips filtration. When no confusion arises, we simply write \mathcal{D}_ℓ instead of $\mathcal{D}_\ell^{(N)}$.

Throughout, we fix a homological degree $\ell \in \mathbb{N}_0$, a positive integer M , a global cutoff $S > 0$ and $\gamma \in [0, 1], \theta \in (0, 1]$ as in Definition 2.

To verify the stability of the proposed PL+JS statistic with respect to variations in the observed data, we prove the continuity of the mapping T_ℓ below.

Theorem 9 *Let $T_\ell: \mathcal{X}^{N_1} \times \mathcal{X}^{N_2} \rightarrow \mathbb{R}$ be the map*

$$T_\ell(x^{(1)}, x^{(2)}) = \Delta_\ell(\mathcal{D}_\ell(x^{(1)}), \mathcal{D}_\ell(x^{(2)})),$$

where $\Delta_\ell: \text{Dgm} \times \text{Dgm} \rightarrow \mathbb{R}$ is the map defined in Definition 2. Equip $\mathcal{X}^{N_1} \times \mathcal{X}^{N_2}$ with the metric

$$d_{\mathcal{X}^{N_1} \times \mathcal{X}^{N_2}}((x^{(1)}, x^{(2)}), (\tilde{x}^{(1)}, \tilde{x}^{(2)})) := d_H^{(N_1)}(x^{(1)}, \tilde{x}^{(1)}) + d_H^{(N_2)}(x^{(2)}, \tilde{x}^{(2)}),$$

where

$$d_H^{(N)}(x, \tilde{x}) := \max \left\{ \max_{1 \leq i \leq N} \min_{1 \leq j \leq N} \|x_i - \tilde{x}_j\|, \max_{1 \leq j \leq N} \min_{1 \leq i \leq N} \|x_i - \tilde{x}_j\| \right\}$$

defines a Hausdorff-type metric on \mathcal{X}^N . Then T_ℓ is $1/2$ -Hölder continuous with respect to this metric:

$$|T_\ell(x^{(1)}, x^{(2)}) - T_\ell(\tilde{x}^{(1)}, \tilde{x}^{(2)})| \leq C_T \sqrt{d_{\mathcal{X}^{N_1} \times \mathcal{X}^{N_2}}((x^{(1)}, x^{(2)}), (\tilde{x}^{(1)}, \tilde{x}^{(2)}))}$$

where

$$C_T := \sqrt{2S C_\phi C_{\text{Density}}},$$

$$C_\phi := \frac{1+\theta}{(\gamma+\theta)\log 2} \left(1 + \frac{2(1-\gamma)}{\theta} \right), \quad C_{\text{Density}} := \frac{8(1-\gamma)}{S^2} \left(\frac{1}{\theta} + \frac{1}{\theta^2} \right).$$

As a preliminary step toward proving Theorem 9, we first verify the continuity of the map $\Delta_\ell: \text{Dgm} \times \text{Dgm} \rightarrow \mathbb{R}$, which appears as a component of T_ℓ .

Proposition 10 *Let*

$$d_\times((D, D'), (\tilde{D}, \tilde{D}')) := d_B(D, \tilde{D}) + d_B(D', \tilde{D}')$$

be the metric on $\text{Dgm} \times \text{Dgm}$ where d_B denotes the bottleneck distance (Appendix A.4). The map

$$\Delta_\ell: \text{Dgm} \times \text{Dgm} \rightarrow \mathbb{R}, \quad (D, D') \mapsto d_{\text{JS}}(p_\ell^{(\gamma, \theta)}(D), p_\ell^{(\gamma, \theta)}(D'))$$

is $1/2$ -Hölder continuous with respect to d_\times . More precisely, for all $(D, D'), (\tilde{D}, \tilde{D}') \in \text{Dgm} \times \text{Dgm}$, we have

$$|\Delta_\ell(D, D') - \Delta_\ell(\tilde{D}, \tilde{D}')| \leq C_\Delta \sqrt{d_\times((D, D'), (\tilde{D}, \tilde{D}'))},$$

where

$$C_\Delta := \sqrt{S C_\phi C_{\text{Density}}},$$

$$C_\phi = \frac{1+\theta}{(\gamma+\theta)\log 2} \left(1 + \frac{2(1-\gamma)}{\theta} \right), \quad C_{\text{Density}} = \frac{8(1-\gamma)}{S^2} \left(\frac{1}{\theta} + \frac{1}{\theta^2} \right).$$

We split the proof into several lemmas.

Lemma 11 (Continuity of the Sum of Persistence Landscapes) *The map*

$$\text{Dgm} \times [0, S] \rightarrow \mathbb{R}, \quad (D, t) \mapsto \Lambda_\ell^{(M)}(D)(t)$$

is continuous, where $\Lambda_\ell^{(M)}$ is defined in Definition 6. Moreover, for all $D, D' \in \text{Dgm}$,

$$\|\Lambda_\ell^{(M)}(D) - \Lambda_\ell^{(M)}(D')\|_\infty \leq M d_B(D, D'). \quad (7)$$

Proof The Lipschitz continuity of each persistence landscape layer with respect to the bottleneck distance is a standard stability result (see, e.g., Bubenik [Bubenik \(2015\)](#)). In particular, for each $m \in \{1, \dots, M\}$,

$$\|\lambda_{\ell,m}(D) - \lambda_{\ell,m}(D')\|_{\infty} \leq d_B(D, D').$$

Hence,

$$\|\Lambda_{\ell}^{(M)}(D) - \Lambda_{\ell}^{(M)}(D')\|_{\infty} \leq \sum_{m=1}^M \|\lambda_{\ell,m}(D) - \lambda_{\ell,m}(D')\|_{\infty} \leq M d_B(D, D').$$

Therefore, the map $\text{Dgm} \rightarrow C([0, S])$, $D \mapsto \Lambda_{\ell}^{(M)}(D)$, is continuous. Since the evaluation map $C([0, S]) \times [0, S] \rightarrow \mathbb{R}$, $(f, t) \mapsto f(t)$, is continuous, the composition $(D, t) \mapsto \Lambda_{\ell}^{(M)}(D)(t)$ is continuous. \square

Lemma 12 (Lipschitz Continuity and Uniform Bounds for the Density) *The density $p_{\ell}^{(\gamma, \theta)}$, defined in Definition 2, satisfies*

$$a_* \leq p_{\ell}^{(\gamma, \theta)}(D)(t) \leq a^*, \quad t \in [0, S], \quad D \in \text{Dgm}, \quad (8)$$

where, in particular, one may take

$$a_* := \frac{\gamma + \theta}{(1 + \theta)S}, \quad a^* := \frac{1}{S} \left(1 + \frac{2(1 - \gamma)}{\theta}\right).$$

Moreover, the map $p_{\ell}^{(\gamma, \theta)}: (\text{Dgm}, d_B) \rightarrow (C([0, S]), \|\cdot\|_{\infty})$, $D \mapsto p_{\ell}^{(\gamma, \theta)}(D)$, is Lipschitz continuous. More precisely, for all $D, D' \in \text{Dgm}$,

$$\|p_{\ell}^{(\gamma, \theta)}(D) - p_{\ell}^{(\gamma, \theta)}(D')\|_{\infty} \leq C_{\text{Density}} d_B(D, D'), \quad (9)$$

where one may take

$$C_{\text{Density}} := \frac{8(1 - \gamma)}{S^2} \left(\frac{1}{\theta} + \frac{1}{\theta^2}\right).$$

Proof Note that, from (6),

$$\|\Lambda_{\ell}^{(M)}(D)\|_{\infty} \leq \frac{1}{2} MS = \frac{2A_{\max}}{S} \quad \text{for all } D \in \text{Dgm}. \quad (10)$$

By Definition 2,

$$p_{\ell}^{(\gamma, \theta)}(D)(t) = (1 - \gamma) \frac{\Lambda_{\ell}^{(M)}(D)(t)}{A_{\ell}(D) + \theta A_{\max}} + \left\{ \gamma + (1 - \gamma) \frac{\theta A_{\max}}{A_{\ell}(D) + \theta A_{\max}} \right\} u_S(t).$$

Since $A_{\ell}(D) \leq A_{\max}$, the coefficient of $u_S(t)$ is bounded below by $\gamma + (1 - \gamma) \frac{\theta}{1 + \theta}$. Hence

$$p_{\ell}^{(\gamma, \theta)}(D)(t) \geq \left(\gamma + (1 - \gamma) \frac{\theta}{1 + \theta}\right) u_S(t) = \frac{\gamma + \theta}{(1 + \theta)S}.$$

For the upper bound, using (10) and $A_{\ell}(D) + \theta A_{\max} \geq \theta A_{\max}$,

$$p_{\ell}^{(\gamma, \theta)}(D)(t) \leq (1 - \gamma) \frac{\frac{2A_{\max}}{S}}{\theta A_{\max}} + u_S(t) = \frac{1}{S} \left(\frac{2(1 - \gamma)}{\theta} + 1\right).$$

Next, write

$$p_{\ell}^{(\gamma, \theta)}(D)(t) - p_{\ell}^{(\gamma, \theta)}(D')(t)$$

$$\begin{aligned}
&= (1 - \gamma) \left(\frac{\Lambda_\ell^{(M)}(D)(t)}{A_\ell(D) + \theta A_{\max}} - \frac{\Lambda_\ell^{(M)}(D')(t)}{A_\ell(D') + \theta A_{\max}} \right) \\
&\quad + (1 - \gamma) \theta A_{\max} \left(\frac{1}{A_\ell(D) + \theta A_{\max}} - \frac{1}{A_\ell(D') + \theta A_{\max}} \right) u_S(t).
\end{aligned}$$

Hence

$$\|p_\ell^{(\gamma, \theta)}(D) - p_\ell^{(\gamma, \theta)}(D')\|_\infty \leq (1 - \gamma) \left(I_1 + \frac{\theta A_{\max}}{S} I_2 \right), \quad (11)$$

where

$$\begin{aligned}
I_1 &:= \left\| \frac{\Lambda_\ell^{(M)}(D)}{A_\ell(D) + \theta A_{\max}} - \frac{\Lambda_\ell^{(M)}(D')}{A_\ell(D') + \theta A_{\max}} \right\|_\infty, \\
I_2 &:= \left| \frac{1}{A_\ell(D) + \theta A_{\max}} - \frac{1}{A_\ell(D') + \theta A_{\max}} \right|.
\end{aligned}$$

From (10) and the triangle inequality, we have

$$\begin{aligned}
I_1 &\leq \left\| \frac{\Lambda_\ell^{(M)}(D) - \Lambda_\ell^{(M)}(D')}{A_\ell(D) + \theta A_{\max}} \right\|_\infty + \left| \frac{1}{A_\ell(D) + \theta A_{\max}} - \frac{1}{A_\ell(D') + \theta A_{\max}} \right| \|\Lambda_\ell^{(M)}(D')\|_\infty \\
&= \frac{\|\Lambda_\ell^{(M)}(D) - \Lambda_\ell^{(M)}(D')\|_\infty}{A_\ell(D) + \theta A_{\max}} + \frac{|A_\ell(D) - A_\ell(D')|}{(A_\ell(D) + \theta A_{\max})(A_\ell(D') + \theta A_{\max})} \frac{2A_{\max}}{S} \\
&\leq \frac{\|\Lambda_\ell^{(M)}(D) - \Lambda_\ell^{(M)}(D')\|_\infty}{\theta A_{\max}} + \frac{2|A_\ell(D) - A_\ell(D')|}{\theta^2 A_{\max}^2 S}.
\end{aligned}$$

Moreover,

$$|A_\ell(D) - A_\ell(D')| \leq \int_0^S |\Lambda_\ell^{(M)}(D)(t) - \Lambda_\ell^{(M)}(D')(t)| dt \leq S \|\Lambda_\ell^{(M)}(D) - \Lambda_\ell^{(M)}(D')\|_\infty,$$

whence

$$\begin{aligned}
I_1 &\leq \frac{1}{A_{\max}} \left(\frac{1}{\theta} + \frac{2}{\theta^2} \right) \|\Lambda_\ell^{(M)}(D) - \Lambda_\ell^{(M)}(D')\|_\infty, \\
I_2 &\leq \frac{|A_\ell(D) - A_\ell(D')|}{\theta^2 A_{\max}^2} \leq \frac{S}{\theta^2 A_{\max}^2} \|\Lambda_\ell^{(M)}(D) - \Lambda_\ell^{(M)}(D')\|_\infty.
\end{aligned}$$

Plugging these into (11) yields

$$\|p_\ell^{(\gamma, \theta)}(D) - p_\ell^{(\gamma, \theta)}(D')\|_\infty \leq \frac{2(1 - \gamma)}{A_{\max}} \left(\frac{1}{\theta} + \frac{1}{\theta^2} \right) \|\Lambda_\ell^{(M)}(D) - \Lambda_\ell^{(M)}(D')\|_\infty.$$

Finally, by $\|\Lambda_\ell^{(M)}(D) - \Lambda_\ell^{(M)}(D')\|_\infty \leq M d_B(D, D')$ (see Lemma 11) and $M = \frac{4A_{\max}}{S^2}$, we obtain (9). \square

Lemma 13 (Continuity of the JS Divergence with respect to Persistence Diagrams) *Let*

$$m(D, D')(t) := \frac{1}{2} (p_\ell^{(\gamma, \theta)}(D)(t) + p_\ell^{(\gamma, \theta)}(D')(t)).$$

The JS divergence with logarithm base 2 can then expressed as

$$\begin{aligned}
\text{JS}(p_\ell^{(\gamma, \theta)}(D) \| p_\ell^{(\gamma, \theta)}(D')) &:= \frac{1}{2} \int_0^S \phi(p_\ell^{(\gamma, \theta)}(D)(t), m(D, D')(t)) dt \\
&\quad + \frac{1}{2} \int_0^S \phi(p_\ell^{(\gamma, \theta)}(D')(t), m(D, D')(t)) dt,
\end{aligned}$$

where

$$\phi(u, v) := u \log_2 \frac{u}{v} = \frac{1}{\log 2} u \log \frac{u}{v}, \quad (u, v) \in (0, \infty)^2.$$

(Throughout, \log denotes the natural logarithm, and \log_2 denotes the base-2 logarithm.) Let

$$d_{\times}((D, D'), (\tilde{D}, \tilde{D}')) := d_B(D, \tilde{D}) + d_B(D', \tilde{D}')$$

be the metric on $\text{Dgm} \times \text{Dgm}$.

Then the map $\text{Dgm} \times \text{Dgm} \rightarrow \mathbb{R}$ defined by $(D, D') \mapsto \text{JS}(p_{\ell}^{(\gamma, \theta)}(D) \| p_{\ell}^{(\gamma, \theta)}(D'))$ is globally Lipschitz continuous with respect to d_{\times} :

$$\left| \text{JS}(p_{\ell}^{(\gamma, \theta)}(D) \| p_{\ell}^{(\gamma, \theta)}(D')) - \text{JS}(p_{\ell}^{(\gamma, \theta)}(\tilde{D}) \| p_{\ell}^{(\gamma, \theta)}(\tilde{D}')) \right| \leq C_{\text{JS}} d_{\times}((D, D'), (\tilde{D}, \tilde{D}')),$$

where

$$C_{\text{JS}} := S C_{\phi} C_{\text{Density}},$$

$$C_{\phi} = \frac{1 + \theta}{(\gamma + \theta) \log 2} \left(1 + \frac{2(1 - \gamma)}{\theta} \right), \quad C_{\text{Density}} = \frac{8(1 - \gamma)}{S^2} \left(\frac{1}{\theta} + \frac{1}{\theta^2} \right).$$

Proof From Lemma 12, for all $t \in [0, S]$ and $D \in \text{Dgm}$,

$$a_* \leq p_{\ell}^{(\gamma, \theta)}(D)(t) \leq a^*,$$

hence also

$$a_* \leq m(D, D')(t) \leq a^*$$

for all $D, D' \in \text{Dgm}$.

We show that ϕ is Lipschitz continuous on the compact rectangle $[a_*, a^*]^2$ with respect to the 1-norm $\|(u, v)\|_1 := |u| + |v|$. Since

$$\frac{\partial \phi}{\partial u}(u, v) = \frac{1}{\log 2} \left(\log \frac{u}{v} + 1 \right), \quad \frac{\partial \phi}{\partial v}(u, v) = -\frac{u}{v \log 2},$$

we have for all $u, v \in [a_*, a^*]$,

$$\begin{aligned} \left| \frac{\partial \phi}{\partial u}(u, v) \right| &\leq \frac{1}{\log 2} \left[\max \left\{ \left| \log \frac{a^*}{a_*} \right|, \left| \log \frac{a_*}{a^*} \right| \right\} + 1 \right] \\ &= \frac{1}{\log 2} \left(\log \frac{a^*}{a_*} + 1 \right) \leq \frac{a^*}{a_* \log 2} = \frac{1 + \theta}{(\gamma + \theta) \log 2} \left\{ 1 + \frac{2(1 - \gamma)}{\theta} \right\} = C_{\phi}, \\ \left| \frac{\partial \phi}{\partial v}(u, v) \right| &\leq \frac{a^*}{a_* \log 2} = C_{\phi}. \end{aligned}$$

Therefore we have for all $(u, v), (u', v') \in [a_*, a^*]^2$,

$$\begin{aligned} |\phi(u, v) - \phi(u', v')| &= \left| \int_0^1 \frac{\partial}{\partial t} \phi(u' + t(u - u'), v' + t(v - v')) dt \right| \\ &\leq \int_0^1 \left| \frac{\partial \phi}{\partial u}(u' + t(u - u'), v' + t(v - v')) (u - u') \right| dt \\ &\quad + \int_0^1 \left| \frac{\partial \phi}{\partial v}(u' + t(u - u'), v' + t(v - v')) (v - v') \right| dt \\ &\leq C_{\phi} (|u - u'| + |v - v'|). \end{aligned} \tag{12}$$

From the inequality (9), we have for all $(D, D'), (\tilde{D}, \tilde{D}') \in \text{Dgm} \times \text{Dgm}$,

$$\|m(D, D') - m(\tilde{D}, \tilde{D}')\|_{\infty} \leq \frac{1}{2} \|p_{\ell}^{(\gamma, \theta)}(D) - p_{\ell}^{(\gamma, \theta)}(\tilde{D})\|_{\infty} + \frac{1}{2} \|p_{\ell}^{(\gamma, \theta)}(D') - p_{\ell}^{(\gamma, \theta)}(\tilde{D}')\|_{\infty}$$

$$\leq \frac{1}{2} C_{\text{Density}} \left(d_B(D, \tilde{D}) + d_B(D', \tilde{D}') \right).$$

Using the inequality (12), we get

$$\begin{aligned} & \left| \text{JS}(p_\ell^{(\gamma, \theta)}(D) \| p_\ell^{(\gamma, \theta)}(D')) - \text{JS}(p_\ell^{(\gamma, \theta)}(\tilde{D}) \| p_\ell^{(\gamma, \theta)}(\tilde{D}')) \right| \\ & \leq \frac{1}{2} \int_0^S \left| \phi(p_\ell^{(\gamma, \theta)}(D)(t), m(D, D')(t)) - \phi(p_\ell^{(\gamma, \theta)}(\tilde{D})(t), m(\tilde{D}, \tilde{D}')(t)) \right| dt \\ & + \frac{1}{2} \int_0^S \left| \phi(p_\ell^{(\gamma, \theta)}(D')(t), m(D, D')(t)) - \phi(p_\ell^{(\gamma, \theta)}(\tilde{D}')(t), m(\tilde{D}, \tilde{D}')(t)) \right| dt \\ & \leq \frac{1}{2} C_\phi \int_0^S \left\{ \left| p_\ell^{(\gamma, \theta)}(D)(t) - p_\ell^{(\gamma, \theta)}(\tilde{D})(t) \right| + \left| m(D, D')(t) - m(\tilde{D}, \tilde{D}')(t) \right| \right\} dt \\ & + \frac{1}{2} C_\phi \int_0^S \left\{ \left| p_\ell^{(\gamma, \theta)}(D')(t) - p_\ell^{(\gamma, \theta)}(\tilde{D}')(t) \right| + \left| m(D, D')(t) - m(\tilde{D}, \tilde{D}')(t) \right| \right\} dt \\ & \leq \frac{1}{2} S C_\phi \left(\left\| p_\ell^{(\gamma, \theta)}(D) - p_\ell^{(\gamma, \theta)}(\tilde{D}) \right\|_\infty + \left\| m(D, D') - m(\tilde{D}, \tilde{D}') \right\|_\infty \right) \\ & + \frac{1}{2} S C_\phi \left(\left\| p_\ell^{(\gamma, \theta)}(D') - p_\ell^{(\gamma, \theta)}(\tilde{D}') \right\|_\infty + \left\| m(D, D') - m(\tilde{D}, \tilde{D}') \right\|_\infty \right) \\ & \leq \frac{1}{2} S C_\phi C_{\text{Density}} \left\{ d_B(D, \tilde{D}) + \frac{1}{2} (d_B(D, \tilde{D}) + d_B(D', \tilde{D}')) \right\} \\ & + \frac{1}{2} S C_\phi C_{\text{Density}} \left\{ d_B(D', \tilde{D}') + \frac{1}{2} (d_B(D, \tilde{D}) + d_B(D', \tilde{D}')) \right\} \\ & = S C_\phi C_{\text{Density}} (d_B(D, \tilde{D}) + d_B(D', \tilde{D}')). \end{aligned}$$

This shows global Lipschitz continuity (hence continuity). \square

Proof of Proposition 10 Since we have

$$|\sqrt{a} - \sqrt{b}| \leq \sqrt{|a - b|}$$

for all $a, b \geq 0$, applying Lemma 13, we have for all $(D, D'), (\tilde{D}, \tilde{D}') \in \text{Dgm} \times \text{Dgm}$,

$$\begin{aligned} |\Delta_\ell(D, D') - \Delta_\ell(\tilde{D}, \tilde{D}')| &= \left| d_{\text{JS}}(p_\ell^{(\gamma, \theta)}(D), p_\ell^{(\gamma, \theta)}(D')) - d_{\text{JS}}(p_\ell^{(\gamma, \theta)}(\tilde{D}), p_\ell^{(\gamma, \theta)}(\tilde{D}')) \right| \\ &= \left| \sqrt{\text{JS}(p_\ell^{(\gamma, \theta)}(D) \| p_\ell^{(\gamma, \theta)}(D'))} - \sqrt{\text{JS}(p_\ell^{(\gamma, \theta)}(\tilde{D}) \| p_\ell^{(\gamma, \theta)}(\tilde{D}'))} \right| \\ &\leq \sqrt{\left| \text{JS}(p_\ell^{(\gamma, \theta)}(D), p_\ell^{(\gamma, \theta)}(D')) - \text{JS}(p_\ell^{(\gamma, \theta)}(\tilde{D}), p_\ell^{(\gamma, \theta)}(\tilde{D}')) \right|} \\ &\leq \sqrt{C_{\text{JS}} d_\times((D, D'), (\tilde{D}, \tilde{D}'))} = C_\Delta \sqrt{d_\times((D, D'), (\tilde{D}, \tilde{D}'))}. \end{aligned}$$

This proves the $1/2$ -Hölder continuity of Δ_ℓ . \square

Before proving Theorem 9, we prepare a standard stability result for Vietoris–Rips persistence diagrams with respect to the Hausdorff distance. This result will serve as a key technical ingredient in the proof.

Proposition 14 (Stability of Vietoris–Rips persistence diagrams) *Let $X, Y \subset \mathbb{R}^d$ be nonempty finite sets, and let $\text{VR}(X) = \{\text{VR}(X, r)\}_{r \geq 0}$ and $\text{VR}(Y) = \{\text{VR}(Y, r)\}_{r \geq 0}$ denote the Vietoris–Rips filtrations parametrized by the diameter, i.e.,*

$$\text{VR}(X, r) := \{\sigma \subset X \mid \max_{x, x' \in \sigma} \|x - x'\| \leq r\}.$$

Then, for each homological degree $\ell \geq 0$, the corresponding persistence diagrams satisfy

$$d_B(D_\ell(\text{VR}(X)), D_\ell(\text{VR}(Y))) \leq 2d_H(X, Y),$$

where d_B denotes the bottleneck distance and d_H the Hausdorff distance.

Proof First, set $\varepsilon := d_H(X, Y)$.

By the definition of the Hausdorff distance, for any $x \in X$ there exists a point $y \in Y$ such that $\|x - y\| \leq \varepsilon$. For each $x \in X$, choose one such point and define $f(x) \in Y$. Similarly, for each $y \in Y$, choose a point $x \in X$ satisfying $\|y - x\| \leq \varepsilon$ and define $g(y) \in X$. Then it follows that $\|x - f(x)\| \leq \varepsilon$ for all $x \in X$, and $\|y - g(y)\| \leq \varepsilon$ for all $y \in Y$.

Fix an arbitrary $r \geq 0$.

Take an arbitrary simplex $\{x_0, \dots, x_k\} \subset X$ contained in $\text{VR}(X, r)$. For any i, j , by the definition of $\text{VR}(X, r)$ we have $\|x_i - x_j\| \leq r$, and hence by the triangle inequality,

$$\|f(x_i) - f(x_j)\| \leq \|f(x_i) - x_i\| + \|x_i - x_j\| + \|x_j - f(x_j)\| \leq r + 2\varepsilon.$$

Therefore, $\{f(x_0), \dots, f(x_k)\}$ is a simplex in $\text{VR}(Y, r + 2\varepsilon)$. This correspondence defines a simplicial map

$$F_r : \text{VR}(X, r) \longrightarrow \text{VR}(Y, r + 2\varepsilon),$$

and similarly a simplicial map

$$G_r : \text{VR}(Y, r) \longrightarrow \text{VR}(X, r + 2\varepsilon).$$

Let $r' \geq r$ be arbitrary. Note that for each simplex $\sigma = \{x_0, \dots, x_k\} \in \text{VR}(X, r)$, we define

$$F_r(\sigma) := \{f(x_0), \dots, f(x_k)\}.$$

Since this definition does not depend on r , for $\sigma \in \text{VR}(X, r')$ we also have

$$F_{r'}(\sigma) = \{f(x_0), \dots, f(x_k)\}.$$

Consequently,

$$F_{r'}(\iota_{r', r}^{(X)}(\sigma)) = F_{r'}(\sigma) = \{f(x_0), \dots, f(x_k)\}.$$

On the other hand,

$$\iota_{r'+2\varepsilon, r+2\varepsilon}^{(Y)}(F_r(\sigma)) = \iota_{r'+2\varepsilon, r+2\varepsilon}^{(Y)}(\{f(x_0), \dots, f(x_k)\}) = \{f(x_0), \dots, f(x_k)\}.$$

Hence, the following diagram commutes for the family $\{F_r\}_{r \geq 0}$:

$$\begin{array}{ccc} \text{VR}(X, r) & \xrightarrow{\iota_{r', r}^{(X)}} & \text{VR}(X, r') \\ F_r \downarrow & & \downarrow F_{r'} \\ \text{VR}(Y, r + 2\varepsilon) & \xrightarrow{\iota_{r'+2\varepsilon, r+2\varepsilon}^{(Y)}} & \text{VR}(Y, r' + 2\varepsilon). \end{array}$$

By the same argument, since the definition of G_r does not depend on the parameter r , the family $\{G_r\}_{r \geq 0}$ also satisfies the corresponding commutativity condition. More precisely, for any $r' \geq r$, the diagram

$$\begin{array}{ccc} \text{VR}(Y, r) & \xrightarrow{\iota_{r', r}^{(Y)}} & \text{VR}(Y, r') \\ G_r \downarrow & & \downarrow G_{r'} \\ \text{VR}(X, r + 2\varepsilon) & \xrightarrow{\iota_{r'+2\varepsilon, r+2\varepsilon}^{(X)}} & \text{VR}(X, r' + 2\varepsilon) \end{array}$$

commutes.

Next, for any simplex $\sigma = \{x_0, \dots, x_k\} \in \text{VR}(X, r)$, the equality

$$\iota_{r+4\varepsilon, r}^{(X)}(\sigma) \cup (G_{r+2\varepsilon} \circ F_r)(\sigma) = \sigma \cup (G_{r+2\varepsilon} \circ F_r)(\sigma)$$

defines a simplex in $\text{VR}(X, r + 4\varepsilon)$. Indeed, this follows from the estimates

$$\begin{aligned} \|x_i - g(f(x_i))\| &\leq \|x_i - f(x_i)\| + \|f(x_i) - g(f(x_i))\| \leq 2\varepsilon, \\ \|x_i - g(f(x_j))\| &\leq \|x_i - x_j\| + \|x_j - f(x_j)\| + \|f(x_j) - g(f(x_j))\| \\ &\leq r + \varepsilon + \varepsilon = r + 2\varepsilon, \\ \|g(f(x_i)) - g(f(x_j))\| &\leq \|g(f(x_i)) - f(x_i)\| \\ &\quad + \|f(x_i) - f(x_j)\| + \|f(x_j) - g(f(x_j))\| \\ &\leq \varepsilon + (r + 2\varepsilon) + \varepsilon = r + 4\varepsilon. \end{aligned}$$

Therefore, the composite map

$$G_{r+2\varepsilon} \circ F_r : \text{VR}(X, r) \rightarrow \text{VR}(X, r + 4\varepsilon)$$

is *contiguous* to the inclusion map $\iota_{r+4\varepsilon, r}^{(X)}$ in $\text{VR}(X, r + 4\varepsilon)$. Similarly, the composite map

$$F_{r+2\varepsilon} \circ G_r : \text{VR}(Y, r) \rightarrow \text{VR}(Y, r + 4\varepsilon)$$

is contiguous to the inclusion $\iota_{r+4\varepsilon, r}^{(Y)}$ in $\text{VR}(Y, r + 4\varepsilon)$.

In general, two contiguous simplicial maps are homotopic on geometric realizations and therefore induce identical maps on homology [Edelsbrunner and Harer \(2010\)](#). Consequently, the homomorphism induced by $G_{r+2\varepsilon} \circ F_r$,

$$(G_{r+2\varepsilon} \circ F_r)_* : H_\ell(\text{VR}(X, r)) \rightarrow H_\ell(\text{VR}(X, r + 4\varepsilon)),$$

coincides with

$$(\iota_{r+4\varepsilon, r}^{(X)})_* : H_\ell(\text{VR}(X, r)) \rightarrow H_\ell(\text{VR}(X, r + 4\varepsilon)).$$

Similarly, the homomorphism induced by $F_{r+2\varepsilon} \circ G_r$,

$$(F_{r+2\varepsilon} \circ G_r)_* : H_\ell(\text{VR}(Y, r)) \rightarrow H_\ell(\text{VR}(Y, r + 4\varepsilon)),$$

coincides with

$$(\iota_{r+4\varepsilon, r}^{(Y)})_* : H_\ell(\text{VR}(Y, r)) \rightarrow H_\ell(\text{VR}(Y, r + 4\varepsilon)).$$

Hence, the persistence modules $\mathbb{X} := \{H_\ell(\text{VR}(X, r))\}_{r \geq 0}$ and $\mathbb{Y} := \{H_\ell(\text{VR}(Y, r))\}_{r \geq 0}$ are 2ε -*interleaved*, and their interleaving distance is at most 2ε .

Since Vietoris–Rips filtrations on finite point sets are finitely generated in each degree, the persistence modules \mathbb{X} and \mathbb{Y} are q -tame. Therefore, by the stability theorem of persistence diagrams [Cohen-Steiner et al. \(2007\)](#), the bottleneck distance d_B and the interleaving distance d_I satisfy

$$d_B(D_\ell(\text{VR}(X)), D_\ell(\text{VR}(Y))) \leq d_I(\mathbb{X}, \mathbb{Y}),$$

and hence

$$d_B(D_\ell(\text{VR}(X)), D_\ell(\text{VR}(Y))) \leq 2\varepsilon = 2d_H(X, Y).$$

This completes the proof. \square

Remark 11 The factor 2 arises from the diameter parametrization of the Vietoris–Rips filtration. For the Čech filtration or for a radius-normalized Vietoris–Rips filtration, the corresponding stability bound holds with constant 1.

Proof of Theorem 9 Applying Proposition 10 and Proposition 14 gives

$$\begin{aligned}
& \left| T_\ell(x^{(1)}, x^{(2)}) - T_\ell(\tilde{x}^{(1)}, \tilde{x}^{(2)}) \right| \\
&= \left| \Delta_\ell(\mathcal{D}_\ell(x^{(1)}), \mathcal{D}_\ell(x^{(2)})) - \Delta_\ell(\mathcal{D}_\ell(\tilde{x}^{(1)}), \mathcal{D}_\ell(\tilde{x}^{(2)})) \right| \\
&\leq C_\Delta \sqrt{d_B(\mathcal{D}_\ell(x^{(1)}), \mathcal{D}_\ell(\tilde{x}^{(1)})) + d_B(\mathcal{D}_\ell(x^{(2)}), \mathcal{D}_\ell(\tilde{x}^{(2)}))} \\
&\leq \sqrt{2} C_\Delta \sqrt{d_H^{(N_1)}(x^{(1)}, \tilde{x}^{(1)}) + d_H^{(N_2)}(x^{(2)}, \tilde{x}^{(2)})}.
\end{aligned}$$

This proves the $1/2$ -Hölder continuity of T_ℓ . \square

Remark 12 (Practical choice of γ and θ) The continuity constant in Theorem 9 reads

$$\begin{aligned}
C_T &= \sqrt{2S C_\phi C_{\text{Density}}}, \\
C_\phi &= \frac{1+\theta}{(\gamma+\theta)\log 2} \left(1 + \frac{2(1-\gamma)}{\theta}\right), \quad C_{\text{Density}} = \frac{8(1-\gamma)}{S^2} \left(\frac{1}{\theta} + \frac{1}{\theta^2}\right).
\end{aligned}$$

Moreover, Lemma 12 yields uniform bounds $a_* \leq p_\ell^{(\gamma, \theta)}(D)(t) \leq a^*$ with $a_* = \frac{\gamma+\theta}{(1+\theta)S}$ and $a^* = \frac{1}{S} \left(1 + \frac{2(1-\gamma)}{\theta}\right)$.

Monotonicity and trade-offs. A direct calculus check shows that, on $(0, 1)$, both C_ϕ and C_{Density} are strictly decreasing in each of γ and θ . Hence C_T decreases as either parameter increases (greater robustness), while the lower bound a_* increases with γ or θ (a stronger floor). At the extremes:

- $\theta \rightarrow 0^+$: C_ϕ , C_{Density} and C_T blow up; the statistic becomes numerically unstable and overly sensitive.
- $\gamma \rightarrow 1^-$: $p_\ell^{(\gamma, \theta)}(D) \rightarrow u_S$ and $\Delta_\ell \equiv 0$; discrimination vanishes.

Parameter management strategy. At the pre-processing stage, we set $S = 1$ by normalizing all attribute vectors with the maximum Euclidean distance among the remaining vectors (i.e., those after excluding outliers). The parameter domains are set to $\theta \in (0, 1]$ and $\gamma \in [0, 1]$; note that $\gamma = 1$ corresponds to the uniform density u_S , for which $\Delta_\ell \equiv 0$. As an efficient rule for parameter management, we basically recommend fixing $\gamma = 0$ and controlling the regularization parameter θ so that the density floor a_* remains above a specified threshold a_{\min} . Given the definition

$$a_* = \frac{\theta}{1+\theta},$$

the condition $a_* \geq a_{\min}$ is equivalent to

$$\theta \geq \frac{a_{\min}}{1-a_{\min}} =: \theta_{\min}.$$

Therefore, by choosing $\theta \geq \theta_{\min}$, one can maintain $a_* \geq a_{\min}$ even with $\gamma = 0$.

In some situations, however, such as small-sample or highly concentrated data, the normalized mass $\mu := A_\ell(D)/A_{\max}$ may become very small. To preserve sensitivity in such cases, it may be desirable to set $\theta < \theta_{\min}$. Then, to maintain $a_* \geq a_{\min}$, a nonzero γ is required. The condition

$$a_* = \frac{\gamma+\theta}{1+\theta} \geq a_{\min}$$

is equivalent to

$$\gamma \geq a_{\min} - (1-a_{\min})\theta =: \gamma_{\min}.$$

Hence, one can choose $\gamma \geq \gamma_{\min}$ to ensure the desired floor level. To enhance discrimination, it is better to set γ to γ_{\min} , but if you want to increase C_T and improve stability, you can achieve this by setting a larger γ .

Numerical example. If $a_{\min} = 0.01$, then

$$\theta_{\min} = \frac{0.01}{1 - 0.01} = 0.0\overline{1}.$$

A simple practical recommendation is to use $(\gamma, \theta) = (0, 0.011)$ as a default configuration. When a smaller $\theta < 0.0\overline{1}$ is required, one may estimate μ (e.g., by the median of a held-out subset) and set $\theta = \mu/10$ together with $\gamma \geq \gamma_{\min} = 0.01 - 0.99\theta$ so that $a_* \geq a_{\min}$ is preserved. This rule keeps the regularization minimal while ensuring numerical stability.

5 Numerical Illustration: Dynamic Point Clouds

Before proceeding to the numerical experiment, we briefly outline the motivation for analyzing the Gitcoin voting data from the perspective of topological data analysis (TDA). The Gitcoin platform is part of the broader *Web3* ecosystem, in which community governance is often implemented through *decentralized autonomous organizations* (DAOs). Unlike traditional organizations with centralized administrators, a DAO operates on a blockchain and makes collective decisions through transparent, rule-based voting mechanisms encoded in smart contracts. Among these, *quadratic voting* (QV) has become a key method: each participant is free to allocate votes across multiple candidates, but the cost of casting v votes increases quadratically (proportional to v^2). This design allows voters to express the *intensity* of their preferences, while imposing a nonlinear budget constraint that encourages diversity of expression and prevents domination by large stakeholders.

The resulting voting data form high-dimensional vectors with rich nonlinear relationships between candidates, reflecting complex collective behaviors within the DAO community. Detecting structural changes in such high-dimensional, nonlinear patterns is crucial for understanding shifts in community preferences or governance dynamics. Because these relationships are inherently geometric and topological in nature, TDA provides an appropriate framework for capturing their evolution. In particular, persistence-based statistics allow us to quantify changes in the topology—such as the emergence or disappearance of clusters or loops—within the cloud of vote vectors over time.

In this section, we conduct empirical verification using the data from the *Gitcoin Steward Council Elections v3* (July 18–25, 2023). (See Appendix C for more information about this data.) The data come from a quadratic voting event conducted over eight days, during which multiple voters cast votes daily for a common set of ten candidates. The ordered sequence of scores that each voter cast for each candidate is referred to as a "vote vector," and is treated as a 10-dimensional attribute vector. Each day within the data period is treated as a separate time window, resulting in eight windows in total. For every pair of adjacent windows, we test whether the corresponding vote vector distributions are generated from the same underlying distribution, following the Monte Carlo permutation-based procedure described in Section D.

Null hypothesis The PL+JS statistics computed from the time windows \mathcal{W}_i and \mathcal{W}_{i+1} are generated from the same distribution.

Alternative hypothesis The PL+JS statistics computed from the time windows \mathcal{W}_i and \mathcal{W}_{i+1} are generated from different distributions.

The pre-processing and parameter settings follow the approach described in Remark 12. Specifically, at the pre-processing stage:

- All pairwise Euclidean distances between vote vectors across all windows are collected.
- The 95th percentile of these distances is taken as q . The remaining 5% are discarded as outliers.
- Every vote vector is rescaled by dividing all its components by q , thereby setting the global cutoff to $S = 1$.

The parameters are fixed to $(\gamma, \theta) = (0, 0.011)$. The PL+JS statistic is computed for homological degrees $\ell = 0$ and $\ell = 1$, each using $M = 3$ persistence landscape layers.

For each adjacent-window pair $(\mathcal{W}_i, \mathcal{W}_{i+1})$ we pool the two daily samples and generate $n = 200$ random labelings that *preserve the original group sizes* (N_i, N_{i+1}) (see Table 1). The Monte Carlo permutation p -value uses the standard “+1 correction” \hat{p}_n (D1). By Proposition 15, these Monte Carlo permutation p -values are *conservative*. We test at a significance level of $\alpha = 0.05$.

Table 1: Daily voter counts and total (Permutation test via Monte Carlo; 8 days)

Date	Number of voters
2023-07-18	350
2023-07-19	601
2023-07-20	197
2023-07-21	244
2023-07-22	268
2023-07-23	342
2023-07-24	443
2023-07-25	187
Total	2632

Monte Carlo precision and empirical p -values.

With $n = 200$ permutations, the worst-case standard error of \hat{p}_n is $1/(2\sqrt{n+1}) = 1/(2\sqrt{201}) \approx 0.035$ from Proposition 16. Moreover, because $\hat{p}_n = (1 + K)/(n + 1)$ with $K \in \{0, \dots, n\}$ the count of exceedances, the attainable p -values lie on the grid $\{1/(n+1), 2/(n+1), \dots, 1\}$ with spacing (grid resolution) $\Delta = 1/(n+1) = 0.004975$. Thus decisions are typically stable unless \hat{p}_n lies very close to $\alpha = 0.05$.

In our adjacent-day tests (Table 2), the H_0 (connected components) p -values for 2023-07-20→2023-07-21 and 2023-07-21→2023-07-22 equal the minimal nonzero value $\Delta = 0.004975$ —i.e., none of the 200 shuffles produced a statistic at least as large as the observed one—so these comparisons strongly reject at $\alpha = 0.05$ and remain significant after Bonferroni adjustment for seven tests ($0.05/7 \approx 0.007$). The preceding pair 2023-07-19→2023-07-20 in H_1 has $\hat{p}_n = 0.069652 = 14\Delta$, which is about 4Δ above $\alpha = 0.05$. Increasing the number of permutations would sharpen the estimate, but it would in any case remain non-significant under Bonferroni. As for other pairs, p -values are mostly well above 0.05 (ranging from 0.15 to 0.92), supporting the temporal stability.

Table 2: Adjacent-day permutation tests (Monte Carlo approximation, $n = 200$). PL+JS statistics and permutation p -values for H_0 and H_1 ; n_1, n_2 are the daily sample sizes.

date ₁	date ₂	$PL + JS_{H_0}$	p_{H_0}	$PL + JS_{H_1}$	p_{H_1}	n_1	n_2
2023-07-18	2023-07-19	0.103 775	0.442 786	0.264 091	0.194 030	350	601
2023-07-19	2023-07-20	0.219 916	0.109 453	0.275 090	0.069 652	601	197
2023-07-20	2023-07-21	0.328 216	0.004 975	0.089 732	0.726 368	197	244
2023-07-21	2023-07-22	0.436 934	0.004 975	0.090 739	0.407 960	244	268
2023-07-22	2023-07-23	0.108 598	0.636 816	0.030 022	0.731 343	268	342
2023-07-23	2023-07-24	0.363 381	0.149 254	0.035 573	0.920 398	342	443
2023-07-24	2023-07-25	0.179 065	0.477 612	0.027 443	0.696 517	443	187

Conclusion.

Taken together, the day-to-day topology of vote vectors is largely stable. Only two adjacent transitions—2023-07-20→2023-07-21 and 2023-07-21→2023-07-22—show statistically significant differences in the H_0 structure (after Bonferroni correction), while no significant changes are detected for H_1 . Given the Monte Carlo grid resolution $\Delta = 1/(n+1) = 1/201$ and worst-case standard error $\leq 1/(2\sqrt{201}) \approx 0.035$, these rejections reflect genuine effects rather than artifacts of simulation noise. We do not attempt to assign causes here; explaining these shifts would require external covariates (e.g., turnout composition or campaign events) and is left for future work.

As discussed in Remark 18, multiple consecutive windows can also be tested jointly using the Holm step-down procedure, which provides higher statistical power than the Bonferroni correction while still controlling the family-wise error rate. In the present analysis, however, even the more conservative Bonferroni adjustment already yielded significant results for these two adjacent transitions. This indicates that the detected changes are sufficiently strong to remain significant under stricter error control.

6 Discussion and Conclusion

6.1 Summary of Contributions

This work develops a probabilistic and computational framework for analyzing persistence statistics in high-dimensional random point clouds. We established moment bounds and tightness results for total and maximum persistence under general distributions, and clarified their scaling behavior within a Gaussian mixture setting. Building on these theoretical foundations, we introduced a bounded, distribution-free statistic—the PL+JS divergence—that combines persistence landscapes with an information-theoretic distance. We proved its $1/2$ –Hölder continuity, providing a rigorous basis for persistence-based comparisons of random point clouds. Illustrative experiments on empirical data demonstrate that the proposed framework can detect meaningful structural transitions in complex systems, but the main contribution of this study lies in its theoretical underpinnings.

6.2 Perspectives for Future Research

Future work will extend the present analysis beyond Gaussian mixtures to more general dependent or non-Euclidean settings, and explore asymptotic regimes for random persistence under various sampling models. Another direction concerns the integration of persistence-based divergences into statistical inference pipelines, including hypothesis testing, change detection, and confidence assessment. From a computational standpoint, efficient approximation of persistence landscapes and their gradients could enable extensions toward optimization and machine-learning applications. Finally, connecting the proposed statistic to interpretable geometric or physical features remains an open challenge, bridging the gap between probabilistic topology and data-driven analysis.

Acknowledgements

The author thanks Dr. Yoshihiko Uchida, Professor at Shunan University, for valuable discussions.

Statements and Declarations

Competing Interests

The author declares that there are no competing interests.

Funding

This research received no external funding.

Data Availability

The datasets used and/or analysed during the current study are available from the corresponding author on reasonable request.

Appendix A An Overview of TDA

This appendix section provides an overview of the basic concepts of TDA, a framework for extracting and quantifying the shape-related features of data, particularly geometric and topological properties such as cluster structures, loops, and voids as discussed in [Carlsson \(2009\)](#); [Edelsbrunner and Harer \(2010\)](#); [Ghrist \(2008\)](#).

A.1 Simplicial Complexes

To endow a discrete set of points with a topological structure, a *simplicial complex* is used. A simplicial complex is a finite set of simplices—points (0-simplices), edges (1-simplices), triangles (2-simplices), tetrahedra (3-simplices), etc.—combined in a way that respects inclusion relations.

Given a discrete point cloud $x = (x_1, \dots, x_N) \in (\mathbb{R}^d)^N$, we can construct a family of simplicial complexes parameterized by a scale parameter $r > 0$. For each fixed r , two representative constructions are the Čech and Vietoris–Rips complexes, which define the connectivity structure of X as scale r .

Čech complex For each data point, consider an open ball of radius $r/2$ centered at that point. A simplex is formed for any set of points whose corresponding balls have a nonempty common intersection. Here, a k -simplex corresponds to a set of $k + 1$ points. The choice of $r/2$ ensures that the Čech complex and the Vietoris–Rips complex (defined below) are built at comparable geometric scales. The Čech complex is known to faithfully capture the topological features of the underlying space (nerve theorem).

Vietoris–Rips complex A k -simplex is formed if all pairwise distances among a set of $k + 1$ points are at most r . Due to its computational efficiency, the Vietoris–Rips complex is often preferred in practice.

A.2 Homology

To extract topological features from a simplicial complex K , *homology* is used.

The space of ℓ -chains over the field $\mathbb{F} := \mathbb{Z}/2\mathbb{Z}$ is defined as:

$$C_\ell(K) := \bigoplus_{\sigma \in K, \dim \sigma = \ell} \mathbb{F}\sigma,$$

where the direct sum is taken over all ℓ -simplices of K .

The *boundary* homomorphism $\partial_\ell: C_\ell(K) \rightarrow C_{\ell-1}(K)$ is defined for $\sigma = \{v_0, v_1, \dots, v_\ell\} \in K$ by:

$$\partial_\ell \sigma = \sum_{i=0}^{\ell} \{v_0, \dots, \hat{v}_i, \dots, v_\ell\} \in C_{\ell-1}(K),$$

where $\hat{\cdot}$ denotes omission.

The *cycle group*, *boundary group*, and *homology group* are given by:

$$\begin{aligned} Z_\ell(K) &:= \text{Ker } \partial_\ell \subset C_\ell(K), \\ B_\ell(K) &:= \text{Im } \partial_{\ell+1} \subset Z_\ell(K), \\ H_\ell(K) &:= Z_\ell(K)/B_\ell(K). \end{aligned}$$

The ℓ -th homology group $H_\ell(K)$ characterizes ℓ -dimensional “holes” (connected components, loops, voids, etc.) in the simplicial complex K . These homology groups form the basis of our topological analysis, as their changing structures directly reflect changes in the underlying geometry of the data. For clarity regarding the geometric and statistical meaning of these features, we adopt the following standard interpretations throughout this paper.

Remark 13 (Interpretation of Homology Elements) For interpretation in the context of statistical data analysis and application to high-dimensional attribute vectors, we use the following standard geometric interpretations:

1. $H_0(K)$: Elements of the 0-th homology group are interpreted as **connected components**. Statistically, these are viewed as **clusters** or distinct groupings within the data.
2. $H_1(K)$: Elements of the 1-st homology group are interpreted as **loops** or circular structures in the data.
3. $H_2(K)$: Elements of the 2-nd homology group are interpreted as **voids** (cavities) or 3-dimensional holes.

A.3 Persistence Diagram

Let $d, N \in \mathbb{N}$ and let $x = (x_1, \dots, x_N) \in (\mathbb{R}^d)^N$ be a finite point cloud in \mathbb{R}^d , where each element of \mathbb{R}^d represents an attribute vector.

The set $K = 2^{\{1, \dots, N\}} \setminus \{\emptyset\}$ corresponds to the simplicial complex consisting of all faces of the $(N-1)$ -simplex.

A *filtration* is a map

$$\Phi = (\Phi_\sigma)_{\sigma \in K} \in \mathbb{R}^{|K|}$$

such that $\Phi_{\sigma_1} \leq \Phi_{\sigma_2}$ whenever $\sigma_1 \subset \sigma_2$ (where \leq denotes the standard order on \mathbb{R}). Here, $|K|$ denotes the cardinality of the set K .

For a given real parameter r , we denote by

$$K_r = \{\sigma \in K : \Phi_\sigma \leq r\}$$

the subcomplex consisting of all simplices whose filtration value is at most r .

For each homological degree $\ell \in \mathbb{N}_0$, there exist an integer $m \in \mathbb{N}_0$, a set of ℓ -chains $\{z_i \in C_\ell(K) : i = 1, \dots, m\}$, and a sequence $((b_i, d_i))_{i=1, \dots, m}$ ($0 \leq b_i \leq d_i \leq \infty$) such that:

1. If $r < b_i$, then $z_i \notin Z_\ell(K_r)$.

2. If $r \geq b_i$, then $z_i \in Z_\ell(K_r)$.
3. If $b_i \leq r < d_i$, then $z_i \notin B_\ell(K_r)$.
4. If $r \geq d_i$, then $z_i \in B_\ell(K_r)$.
5. For each i with $b_i \leq r < d_i$, the homology classes of z_i in $H_\ell(K_r)$ form a basis of $H_\ell(K_r)$.

Remark 14 This is classical; see [Edelsbrunner et al. \(2002\)](#); [Edelsbrunner and Harer \(2010\)](#); [Ghrist \(2008\)](#). For stability of barcodes under perturbations of the filtration, see [Cohen-Steiner et al. \(2007\)](#).

Each pair (b_i, d_i) may have multiplicity and is referred to as a *birth-death pair* (or bar). The birth-death pairs $((b_i, d_i))_{i=1, \dots, m}$ are regarded as a locally finite multisets on $\{(b, d) \in \bar{\mathbb{R}}^2 : b < d\}$ with the convention that the diagonal $\{(t, t) : t \in \bar{\mathbb{R}}\}$ has infinite multiplicity. The finite multiset D is called the *persistence diagram* (or barcode) in degree ℓ (see, e.g., [Edelsbrunner et al. \(2002\)](#); [Cohen-Steiner et al. \(2007\)](#)).

A.4 Bottleneck Distance

The bottleneck distance was introduced by [Cohen-Steiner et al. \(2007\)](#), a standard metric on persistence diagrams that quantifies the largest deviation between features of two diagrams under optimal matching. This distance plays a central role in stability results for persistent homology.

In what follows, we reuse the notation introduced in Section 3.1.

Definition 3 (Bottleneck Distance) Let $D, D' \in \text{Dgm}$ be persistence diagrams in degree ℓ .

A *matching* Γ between D and D' is a subset

$$\Gamma \subset D \times D'$$

such that the coordinate projections

$$\pi_1 : \Gamma \rightarrow D, \quad \pi_2 : \Gamma \rightarrow D'$$

are bijections onto their respective diagrams after adding diagonal points. Unmatched points are allowed to be paired with point in the diagonal ($\Delta := \{(b, d) \in \bar{\mathbb{R}}^2 : b = d\}$).

The *cost* of Γ is defined by

$$\text{cost}(\Gamma) := \sup_{(p, q) \in \Gamma} \|p - q\|_\infty, \quad \|(b, d)\|_\infty := \max\{|b|, |d|\}.$$

The *bottleneck distance* in degree ℓ is

$$d_{\ell, B}(D, D') := \inf_{\Gamma} \text{cost}(\Gamma),$$

where the infimum runs over all matchings Γ .

Remark 15 Infinite multiplicity on Δ ensures that a matching always exists by allowing any leftover point to be paired with a diagonal point (interpreting zero-length features as noise).

A.5 Persistence Landscape

Persistence diagrams provide a finite multiset representation of topological features, but for certain analytical and statistical purposes, it is often more convenient to work with a functional summary. The *persistence landscape*, introduced by [Bubenik \(2015\)](#), transforms a persistence diagram into a sequence of piecewise-linear functions, enabling the use of functional analysis and statistical tools while retaining key topological information. We recall its definition below, following the notation in Section 3.1.

For each point (b, d) ($d < \infty$) in a persistence diagram D in degree $\ell \in \mathbb{N}_0$, we define a triangular-shaped function supported on the interval $[b, d]$, with its maximum value attained at the midpoint $\frac{b+d}{2}$, as follows:

$$f_{(b,d)}(t) = \begin{cases} t - b & \text{if } b \leq t \leq \frac{b+d}{2}, \\ d - t & \text{if } \frac{b+d}{2} < t \leq d, \\ 0 & \text{otherwise} \end{cases}$$

This function takes positive values only on the interval $[b, d]$ and forms a symmetric triangular function whose peak height is $\frac{d-b}{2}$.

For any $t \in \mathbb{R}$, let the m -th largest value be

$$\lambda_{\ell,m}(D)(t) = m\text{-}\max\{f_{(b,d)}(t) : (b, d) \in D\}.$$

Here note that D has finite elements. The function $\lambda_{\ell,m}(D)$ is called the m -th persistence landscape layer, and the sequence $(\lambda_{\ell,m}(D))_{m \in \mathbb{N}_0}$ is referred to as the *persistence landscape*.

Appendix B JS Divergence

For completeness, we briefly recall the definition of the Jensen–Shannon (JS) divergence, which is used in the construction of the PL+JS statistic in the main text. The JS divergence is a symmetrized and smoothed variant of the Kullback–Leibler (KL) divergence, and is widely used as a finite and symmetric measure of dissimilarity between probability distributions. Throughout this paper, we compute divergences using logarithm base 2. This choice is twofold: first, it expresses the divergence in *bits*, which is standard in information theory; second, it normalizes the maximum possible JS divergence to 1, which makes the JS distance lie in the range $[0, 1]$ and facilitates interpretation. We begin by recalling the definition of the KL divergence, which quantifies the discrepancy between two probability density functions in an asymmetric manner.

Definition 4 Let p and q be probability density functions with respect to a common reference measure μ . The *Kullback–Leibler (KL) divergence* of p from q , computed with logarithm base 2, is defined as

$$\text{KL}(p\|q) := \int_{\{q(t)>0\}} p(t) \log_2 \frac{p(t)}{q(t)} d\mu(t).$$

We adopt the following conventions for the integrand:

- If $p(t) = 0$, then $p(t) \log_2 \frac{p(t)}{q(t)}$ is taken to be 0.
- If $q(t) = 0$ and $p(t) > 0$ on a set of positive μ -measure, then $\text{KL}(p\|q) = +\infty$.

Definition 5 Let p and q be probability density functions. The *Jensen-Shannon (JS) divergence* is defined as

$$\text{JS}(p\|q) := \frac{1}{2} \text{KL}(p\|m) + \frac{1}{2} \text{KL}(q\|m),$$

where m is the density of the mixture distribution

$$m(t) = \frac{1}{2}(p(t) + q(t)).$$

Since $m(t) > 0$ whenever $p(t) > 0$ or $q(t) > 0$, both terms in the definition are finite, and hence $\text{JS}(p\|q) < \infty$.

Definition 6 For two probability density functions p and q , the Jensen-Shannon distance, computed with logarithm base 2, is defined as

$$d_{\text{JS}}(p, q) = \sqrt{D_{\text{JS}}(p\|q)}.$$

Appendix C Empirical Analysis: A Case Study on Web3 Voting Behavior

In appendix section, we describe the preprocessing procedure applied to the *Gitcoin Steward Council Elections v3* dataset used in Section 5. We then clarify the characteristics of the data through principal component analysis (PCA) and Gaussian mixture model (GMM) fitting, and finally conduct simulations to empirically verify the validity of Corollary 8.

C.1 Dataset and Methods

This study analyzes the voting data from the Gitcoin Steward Council Elections v3, held from July 18 to July 25, 2023. The data were collected via the “GraphQL API” provided by Snapshot, a decentralized voting platform, by accessing <https://hub.snapshot.org/graphql>. We searched for the proposal titled “Gitcoin Steward Council Elections v3” submitted by the community `gitcoindao.eth`, and developed a Python script to automatically retrieve all voting records associated with this proposal.

Each voting record contains the voter’s address, timestamp, and the score allocation for each candidate. The dataset, originally in nested JSON format, was transformed into a flat tabular structure using `pandas.json_normalize()` and subsequently stored in CSV format for further analysis. It covers an eight-day period, from July 18 to July 25, 2023, and consists of 2,632 records. The columns `choice.1` through `choice.10` represent the scores assigned by each voter to each candidate, and the sequence of these ten scores is referred to as the vote vector, indicating how each voter distributed their scores among multiple candidates.

Our analytical procedure proceeds in two steps: (1) As a preliminary step before conducting TDA, we initially apply principal component analysis (PCA) to examine the contribution of the linear components of the data, evaluating the cumulative

explained variance and principal components. (2) Fit a GMM to capture latent clusters of voting behavior, and conduct simulations by controlling the variance scaling parameter η . This enables us to examine how persistence statistics (total and maximum persistence) evolve as dispersion grows, linking directly to the theoretical results on variance scaling.

C.2 PCA

We first center each voter's 10-dimensional vector of scores for the candidates (by subtracting the mean vector shown in Table 4) and apply principal component analysis (PCA). The results are presented in Tables 5 and 6.

According to the mean vector in Table 4, Candidate 1 has the highest mean score (approximately 4.29), significantly exceeding the others, followed by Candidate 2 (1.34) and Candidate 4 (1.17). This indicates that, overall, there is strong support for Candidate 1, while Candidates 2 and 4 also receive a non-negligible share of votes.

From the eigenvalues and variance ratios in Table 5, the proportion of variance explained by the first principal component is about 58%, followed by 12% for the second, 7.7% for the third, and 6.2% for the fourth. The cumulative contribution rate reaches 78% with three components and 91% with six components.

The first eigenvector (PC1) has a very large positive loading for Candidate 1 (about 0.99), while the loadings for other candidates are all 0.13 or less (Table 6). Thus, the first principal component strongly reflects the magnitude of the score for Candidate 1, with higher PC1 scores corresponding to voters who concentrate their scores on Candidate 1.

The second eigenvector (PC2) has a large positive loading for Candidate 4 (about 0.77), and relatively large values for Candidates 2, 5, 3 and 6, while Candidate 1 has a negative loading (-0.11). Hence, the second principal component represents an axis contrasting “emphasis on Candidates 4, 2, and 5” versus “emphasis on Candidate 1.”

The third eigenvector (PC3) has the largest positive loading for Candidate 2 (about 0.80) and a large negative loading for Candidate 4 (-0.52). This axis represents another pattern contrasting “emphasis on Candidate 2” versus “emphasis on Candidate 4.”

In summary, the voting structure of this dataset can be characterized by three main axes:

- PC1: Concentration on Candidate 1
- PC2: Candidates 4 (and 2, 5) vs Candidate 1
- PC3: Candidate 2 vs Candidate 4

The patterns suggested by PC1–PC3 indicate distinct archetypes of scoring behavior. To operationalize this structure, we model the vote vectors as a GMM, which may provide probabilistic cluster memberships aligned with these axes.

C.3 GMM

To investigate how the characteristics of voting behavior affect the topology, we construct a simulation model of the voting behavior.

Table 4: Mean Vector of Voting Scores

Candidate	Mean Score
choice.1	4.29
choice.2	1.34
choice.3	0.88
choice.4	1.17
choice.5	0.73
choice.6	0.66
choice.7	0.51
choice.8	0.41
choice.9	0.46
choice.10	0.50

Table 5: Eigenvalues and Variance Ratios (PCA Results)

Principal Component	Eigenvalue	Variance Ratio	Cumulative
PC1	222.38	58%	58%
PC2	45.93	12%	70%
PC3	29.47	7.7%	78%
PC4	23.68	6.2%	84%
PC5	15.64	4.1%	88%
PC6	12.10	3.2%	91%
PC7	10.39	2.7%	94%
PC8	9.18	2.4%	96%
PC9	8.71	2.3%	99%
PC10	4.99	1.4%	100%

Table 6: Principal Component Loadings

	choice.1	choice.2	choice.3	choice.4	choice.5	choice.6	choice.7	choice.8	choice.9	choice.10
PC1	0.99	0.13	0.05	0.05	0.01	0.00	0.01	0.01	0.02	0.02
PC2	-0.11	0.38	0.24	0.77	0.30	0.24	0.15	0.08	0.08	0.10
PC3	-0.10	0.80	0.27	-0.52	0.06	-0.02	-0.01	0.03	0.02	0.04
PC4	0.03	-0.29	0.08	-0.35	0.47	0.52	0.32	0.23	0.34	0.08
PC5	0.00	-0.25	0.81	-0.02	-0.39	0.28	-0.20	-0.10	-0.07	0.03
PC6	-0.02	0.05	-0.08	0.05	-0.54	-0.13	0.32	0.05	0.60	0.46
PC7	0.00	-0.21	0.34	-0.03	0.41	-0.64	-0.02	0.14	-0.08	0.48
PC8	0.01	0.05	-0.27	-0.05	-0.06	0.39	-0.14	-0.06	-0.48	0.72
PC9	-0.01	0.03	-0.12	0.04	0.08	0.08	-0.83	0.30	0.43	0.08
PC10	0.00	0.01	0.01	0.02	-0.26	-0.02	0.14	0.90	-0.30	-0.11

The Gitcoin Steward Council Elections v3 voting data consist of Quadratic Voting for $d = 10$ candidates by $N = 2632$ voters. The vote vector of voter i , representing the number of votes for each candidate, is given by

$$x_i = (x_{i1}, x_{i2}, \dots, x_{i,10})^\top \in \mathbb{R}^{10}, \quad i = 1, \dots, N.$$

We assume that these vote vectors are independent samples drawn from a K -component GMM in 10-dimensional space \mathbb{R}^{10} , where K is the number of clusters. As we have seen in Section 3.4, which defines the GMM, the parameters are $\{\pi_k, \mu_k, \Sigma_k\}_{k=1}^K$. We estimate these parameters by maximum likelihood (EM algorithm) using scikit-learn’s `GaussianMixture` with *full covariance matrices* (i.e., each component has its own unrestricted positive-definite covariance matrix, allowing arbitrary cluster shapes and orientations) and `n_init = 10` random initializations to mitigate the risk of convergence to poor local optima.

To determine the number of components K , we evaluate candidate values $K = 1, \dots, 10$, fitting a GMM for each and computing the Bayesian and Akaike information criteria (BIC/AIC). Although both BIC and AIC continue to decrease slightly beyond $K = 6$, we adopt $K = 6$ as a parsimonious choice that balances model fit and simplicity. As a sanity check, we generate synthetic samples from the fitted $K = 6$ model using its estimated $\{\pi_k, \mu_k, \Sigma_k\}$ and repeat the same BIC/AIC evaluation; the resulting profiles closely align with those from the real data (see Figure 1). Here, “real” refers to the observed vote vector data. The number of synthetic samples in each cluster is determined according to π_k , and the samples are drawn from the multivariate normal distribution $\mathcal{N}(\mu_k, \Sigma_k)$. Comparing the BIC/AIC curves for real and synthetic data allows us to verify whether the fitted GMM reproduces the cluster structure of the real data; in our case, both exhibit similar decreasing trends with a clear elbow at $K = 6$.

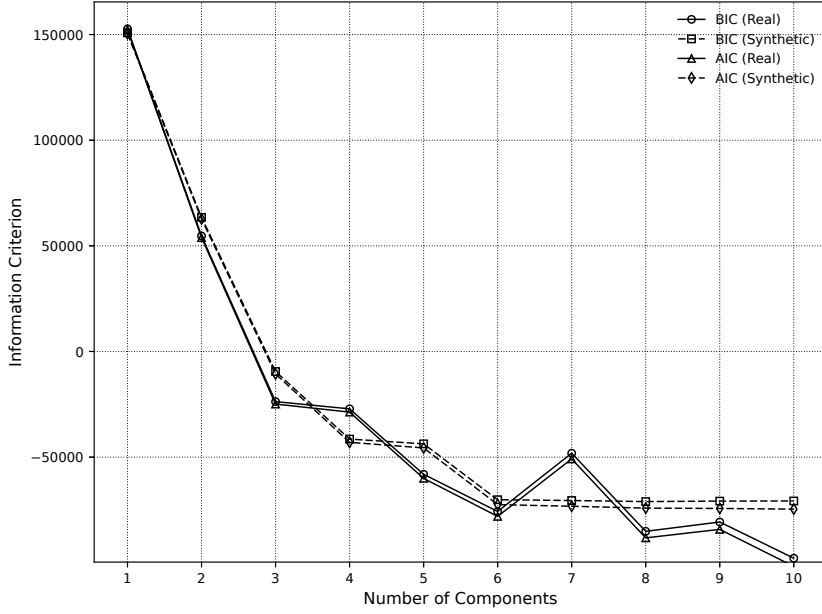


Fig. 1: Comparison of cluster number selection by BIC and AIC (Real vs Synthetic)

The final model selected is a GMM with $K = 6$ components. Tables 7 and 8 summarize the estimated parameters of each component. For readability, the results are split into two tables: Table 7 reports the square roots of the minimum ¹ and maximum eigenvalues of the covariance matrices, the mixture weights, and the first four entries of the mean vector, while Table 8 shows the remaining mean vector entries. Components 2, 5, and 6 are nearly degenerate, with very small minimum eigenvalues, indicating that the distribution is effectively confined to a lower-dimensional subspace. The coexistence of nearly degenerate components (2, 5, and 6) and more diffuse components (1, 3, and 4) suggests heterogeneity in decision-making styles:

Table 7: Summary Statistics of GMM Components – 1

Component	sqrt_min	sqrt_max	weight	choice.1	choice.2	choice.3	choice.4
1	0.4	1.0	0.28	0.6	0.5	0.4	0.5
2	0.0	20.5	0.34	6.3	0.0	0.0	0.0
3	0.7	11.0	0.05	7.1	3.5	4.2	2.3
4	5.6	25.0	0.02	19.1	6.8	3.1	6.5
5	0.0	34.0	0.03	25.6	16.0	12.1	21.8
6	0.0	8.1	0.27	1.6	1.5	0.5	0.5

Table 8: Summary Statistics of GMM Components – 2

Cluster	choice.5	choice.6	choice.7	choice.8	choice.9	choice.10
1	0.4	0.5	0.4	0.4	0.4	0.5
2	0.0	0.0	0.0	0.0	0.0	0.0
3	2.2	2.0	1.7	1.9	1.8	2.5
4	7.0	6.9	5.9	7.8	10.4	9.6
5	10.6	8.6	5.4	0.1	0.0	0.1
6	0.0	0.0	0.0	0.0	0.0	0.0

C.4 Effect of Variance Scaling on Model Fit and persistence statistics

We now investigate how scaling the covariance matrices in the fitted $K = 6$ GMM affects both model fit and the topology of the generated point clouds. For a given scale factor $\eta > 0$, the covariance matrices Σ_k are replaced with $\eta \Sigma_k$, and synthetic samples are drawn from the resulting model.

From the topological perspective, we focus on four quantities derived from the definitions in Section 3.1 and the mathematical results in Theorem 5 or Corollary 8:

¹Note that the entries shown as 0.0 are not exactly zero but small positive values. The GaussianMixture implementation in scikit-learn applies internal regularization and numerical stabilization, ensuring that the covariance matrices remain positive definite and effectively preventing true zero (singular) eigenvalues. See Remark 4 (i).

- *Sum H0 Bar*: the total persistence of H_0 bars ($\mathcal{L}_{0,\text{total}}$).
- *Sum H1 Bar*: the total persistence of H_1 bars ($\mathcal{L}_{1,\text{total}}$).
- *Max H0 Bar*: the maximum persistence of H_0 bars ($\mathcal{L}_{0,\text{max}}$).
- *Max H1 Bar*: the maximum persistence of H_1 bars ($\mathcal{L}_{1,\text{max}}$).

Figures 2 and 3 plot these persistence statistics together with the mean log-likelihood as functions of the scale factor η . Here, by “log-likelihood” we mean the pointwise log-density of the fitted GMM $\theta = \{\pi_k, \mu_k, \Sigma_k\}_{k=1}^K$ evaluated at a data point $x \in \mathbb{R}^{10}$:

$$f(\theta; x) := \log \left(\sum_{k=1}^K \pi_k \varphi(x \mid \mu_k, \Sigma_k) \right),$$

here $\varphi(\cdot \mid \mu_k, \Sigma_k)$ is the Gaussian density with mean μ_k and covariance Σ_k .

For each η , we generate synthetic samples $x'_1(\eta), \dots, x'_N(\eta)$ from the fitted GMM with covariances scaled by a factor η (i.e., $\Sigma_k \mapsto \eta \Sigma_k$ while keeping (π_k, μ_k) fixed), using the same sample size N as the original dataset, and we report the mean log-likelihood

$$\bar{f}(\eta) = \frac{1}{N} \sum_{j=1}^N f(\theta; x'_j(\eta)).$$

In Figures 2 and 3, this quantity $\bar{f}(\eta)$ is plotted.

The mean log-likelihood decreases almost monotonically as η increases. This is expected: enlarging each component’s covariance draws more dispersed samples, which lowers the predictive density under the fixed fitted model.

Regarding the persistence statistics, the results are consistent with the bounds in Theorem 5 or Corollary 8. In particular:

- *Sum H0 Bar and Max H0 Bar* increases rapidly for small η and then plateaus, reflecting the $\mathcal{O}(\eta^{1/2})$ growth predicted by Corollary 8.
- *Sum H1 Bar and Max H1 Bar* exhibits larger fluctuations, especially for small η , consistent with the sensitivity of H_1 features to noise and the sparser appearance of loops in the data.

Overall, the empirical trends of both H_0 and H_1 metrics align qualitatively with the $\eta^{1/2}$ -order bounds in Corollary 8.

Appendix D Change-Point Detection Methods

This appendix section provides the methodological details used in Section 5 to empirically assess the effectiveness of the PL+JS statistic. We lay out the hypothesis–testing workflow, the permutation (and Monte Carlo) procedure, and the assumptions required for validity, together with remarks on multiple testing control. While illustrative examples are drawn from Gitcoin voting data and financial time series, the proposed framework and testing procedure are general and applicable to a broad class of high-dimensional dynamic systems. These materials serve as the technical reference for the empirical analyses reported in the main text.

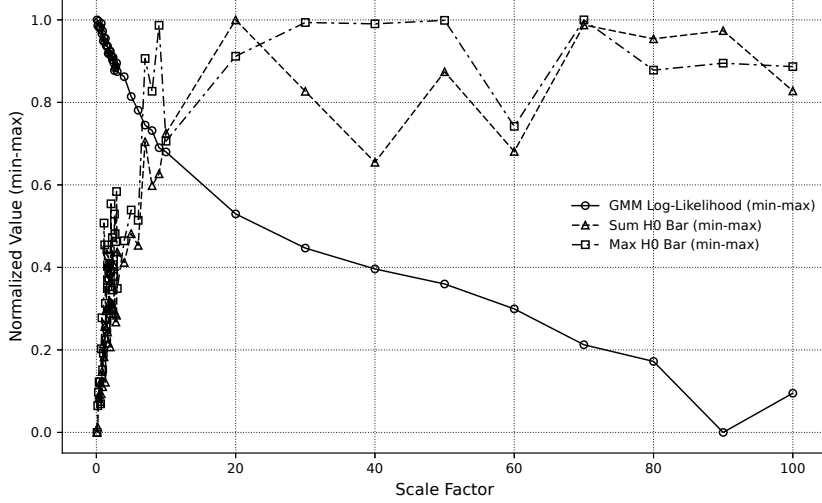


Fig. 2: Scale factor vs. GMM log-likelihood and H_0 persistence statistics

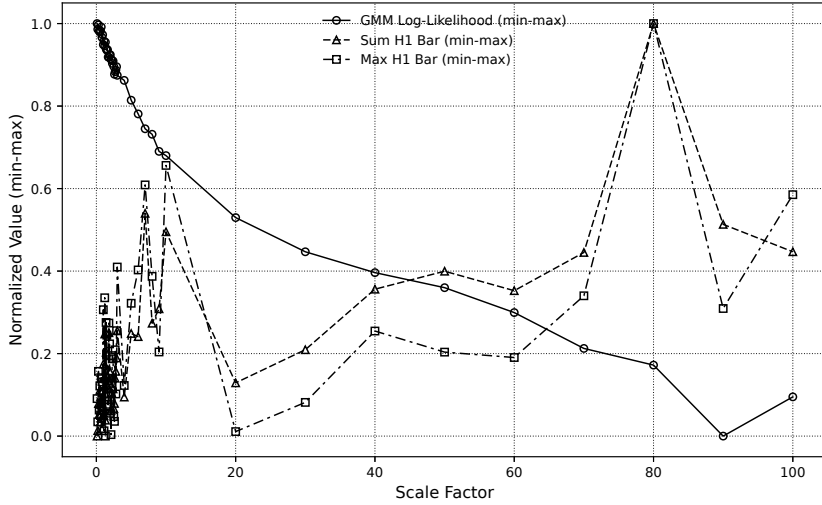


Fig. 3: Scale factor vs. GMM log-likelihood and H_1 persistence statistics

D.1 Hypothesis Testing Algorithm

Let \mathcal{W}_1 and \mathcal{W}_2 denote two time windows, each consisting of multiple attribute vectors. A time series of attribute vectors can be divided into multiple windows, and for each window, a persistence diagram is computed to capture the underlying topological structure. By comparing the persistence diagrams corresponding to different windows, we can detect structural changes in the data-generating process over time. Examples

of such windows include, for instance, all vote vectors observed on each voting day in the case of DAO, or all daily return vectors within each month in the case of asset price data. The goal is to test whether the topological structure of \mathcal{W}_1 differs significantly from that of \mathcal{W}_2 .

We can compare the two persistence diagrams obtained from \mathcal{W}_1 and \mathcal{W}_2 using the PL+JS statistic defined in Definition 2, and perform a permutation test (or its Monte Carlo approximation) to examine whether the attribute-vector structures in the two time windows are drawn from the same distribution.

Null hypothesis The PL+JS statistics computed from the time windows \mathcal{W}_1 and \mathcal{W}_2 are generated from the same distribution.

Alternative hypothesis The PL+JS statistics computed from the time windows \mathcal{W}_1 and \mathcal{W}_2 are generated from different distributions.

The detailed computation procedure by Monte Carlo is shown in Algorithm 1.

Algorithm 1 Computation of the permutation p -value

```

Input: Number of attribute vectors:  $N_1$  from  $\mathcal{W}_1$ ,  $N_2$  from  $\mathcal{W}_2$ 
 $V_1 \leftarrow$  set of attribute vectors from  $\mathcal{W}_1$ 
 $V_2 \leftarrow$  set of attribute vectors from  $\mathcal{W}_2$ 
 $true\_dist \leftarrow$  PL+JS statistic from persistence diagrams of  $V_1$  and  $V_2$ 
 $all\_vectors \leftarrow \text{concat}(V_1, V_2)$ 
 $dist\_list \leftarrow []$  ▷ empty list
 $count \leftarrow 0$ 
while  $count <$  number of shuffles do
     $U_1, U_2 \leftarrow$  randomly select  $N_1$  and  $N_2$  vectors from  $all\_vectors$  (without
    replacement)
     $dist \leftarrow$  PL+JS statistic computed from persistence diagrams of  $U_1$  and  $U_2$ 
    append  $dist$  to  $dist\_list$ 
     $count \leftarrow count + 1$ 
end while
 $p\_val \leftarrow \frac{1 + |\{d \in dist\_list : d \geq true\_dist\}|}{\text{number of shuffles} + 1}$ 
Output:  $p\_val$ 

```

D.2 Assumptions, Validity, and Error Control for Permutation Testing

This subsection complements the algorithmic description in Section 1 by detailing the assumptions required for the validity of the permutation framework, its theoretical guarantees (conservativeness and exchangeability), and practical issues such as Monte Carlo accuracy and multiple-testing control.

Let $(\Omega, \mathcal{F}, \mathbb{P})$ be a probability space. Let \mathcal{W}_1 and \mathcal{W}_2 be any two distinct time windows. For $k \in \{1, 2\}$, let

$$X_1^{(k)}, \dots, X_{N_k}^{(k)} : \Omega \rightarrow \mathcal{X}$$

be i.i.d. random variables sharing the same distribution P_k under \mathbb{P} . (Here, “i.i.d.” means that the random variables are independent and identically distributed with respect to \mathbb{P} .) Each realization of $X_i^{(k)}$ represents one attribute vector from \mathcal{W}_k . Note that in this section we do not impose any specific assumptions on the probability distributions; in particular, we do not assume them to follow a GMM as considered in Section 3.4. We denote by

$$X^{(k)} := (X_1^{(k)}, \dots, X_{N_k}^{(k)}) \in \mathcal{X}^{N_k}$$

the sample of attribute vectors from \mathcal{W}_k .

Our aim is to test the null hypothesis

$$H_{\text{null}} : P_1 = P_2$$

against the alternative

$$H_{\text{alt}} : P_1 \neq P_2.$$

In other words, we investigate whether the distribution of attribute vectors from \mathcal{W}_1 coincides with that from \mathcal{W}_2 . Rejecting the null hypothesis indicates that the collective voting behavior has significantly changed between the two time windows. To assess this, we employ a permutation test with Monte Carlo approximation, using the PL+JS statistic introduced in Definition 2 as a measure of discrepancy between the two empirical samples.

To mathematically formulate the permutation test, we introduce the following notation.

Definition 7 For $x = (x_1, \dots, x_{N_1}) \in \mathcal{X}^{N_1}$ and $y = (y_1, \dots, y_{N_2}) \in \mathcal{X}^{N_2}$, define the concatenation operator

$$\text{concat} : \mathcal{X}^{N_1} \times \mathcal{X}^{N_2} \rightarrow \mathcal{X}^{N_1+N_2}$$

by

$$\text{concat}(x, y) := (x_1, \dots, x_{N_1}, y_1, \dots, y_{N_2}).$$

Using this notation, the *pooled sample* associated with the random vectors $X^{(1)}$ and $X^{(2)}$ is defined as

$$Z = (Z_1, \dots, Z_{N_1+N_2}) := \text{concat}(X^{(1)}, X^{(2)}) \in \mathcal{X}^{N_1+N_2}.$$

Let us recall the notion of exchangeability.

Definition 8 (Exchangeability) Let $Z = (Z_1, \dots, Z_{N_1+N_2}) \in \mathcal{X}^{N_1+N_2}$ be random vector on the probability space $(\Omega, \mathcal{F}, \mathbb{P})$. We say that Z is *exchangeable* if for every permutation π of $\{1, \dots, N_1 + N_2\}$,

$$(Z_1, \dots, Z_{N_1+N_2}) \stackrel{d}{=} (Z_{\pi(1)}, \dots, Z_{\pi(N_1+N_2)}),$$

where $\stackrel{d}{=}$ denotes equality in distribution.

To ensure that the pooled sample Z is exchangeable under the above setting, we impose the following assumption.

Assumption 2 (independence across time windows) The two samples are independent as random vectors: $\sigma[X^{(1)}]$ and $\sigma[X^{(2)}]$ are independent (equivalently, $(X^{(1)}, X^{(2)}) \sim P_1^{\otimes N_1} \otimes P_2^{\otimes N_2}$).

Under the hypothesis $H_{\text{null}} : P_1 = P_2 =: P$, the pooled sample Z has independent and identically distributed components with common distribution P ; equivalently, the joint distribution of Z is $P^{\otimes(N_1+N_2)}$. Hence Z is exchangeable.

Remark 16 (Independence of Vote Vectors) When the attribute vectors represent vote vectors (e.g., in the Gitcoin dataset), the independence—both among voters within each time window and between time windows—is natural, because each voter makes an individual decision and each voting round or day is regarded as an independent event. In most Web3 governance platforms (e.g., Snapshot), however, the ongoing voting outcomes are publicly visible during the voting period, which may induce weak social dependence among voters. Such transparency can lead to minor correlations in voting behavior, yet these effects are typically limited compared with the heterogeneity of individual vote vectors, so that the assumption of approximate independence remains reasonable for statistical testing.

Remark 17 (Independence of Financial Attribute Vectors) When the attribute vectors represent financial quantities such as asset prices or interest rates, the raw levels typically exhibit strong temporal dependence. To approximate independence both within and between time windows, it is more appropriate to use return-type or difference-type vectors. For asset prices, one may consider the simple return

$$R_t^{(i)} = \frac{S_t^{(i)} - S_{t-1}^{(i)}}{S_{t-1}^{(i)}} \quad \text{or} \quad R_t^{(i)} = \frac{S_t^{(i)}}{S_{t-1}^{(i)}} - 1,$$

or the log-return

$$r_t^{(i)} = \log S_t^{(i)} - \log S_{t-1}^{(i)}.$$

For interest rates (or yields), which are already expressed as ratios or percentages, it is more appropriate to use difference-type measures such as

$$\Delta r_t^{(i)} = r_t^{(i)} - r_{t-1}^{(i)},$$

representing daily or monthly changes in the rate level. Using these transformed vectors mitigates serial dependence and makes the independence assumption across samples more reasonable.

Let us consider the family of index subsets

$$\mathcal{H} := \{ h \subset \{1, \dots, N_1 + N_2\} : |h| = N_1 \}.$$

Here, $|h|$ denotes the cardinality of the set h . Thus, \mathcal{H} consists of all subsets of $\{1, \dots, N_1 + N_2\}$ having exactly N_1 elements. In particular, $|\mathcal{H}| = \binom{N_1 + N_2}{N_1}$.

For each $h \in \mathcal{H}$, write $h^c := \{1, \dots, N_1 + N_2\} \setminus h$ and define the *split* of the pooled sample

$$Z_h := (Z_i)_{i \in h} \in \mathcal{X}^{N_1}, \quad Z_{h^c} := (Z_i)_{i \in h^c} \in \mathcal{X}^{N_2}.$$

Define the permuted statistic $\mathcal{T}_h(Z) := T_\ell(Z_h, Z_{h^c})$. Let $h_0 := \{1, \dots, N_1\}$ denote the original labeling so that $\mathcal{T}_{h_0}(z)$ is the observed statistic.

In the following, we provide the definitions of both the exact p -value of the permutation test and the Monte Carlo p -value obtained via Monte Carlo approximation.

Definition 9 (Exact Permutation p -Value) The exact permutation p -value of the permutation test is

$$p_{\text{exact}}(Z) := \frac{1}{|\mathcal{H}|} \sum_{h \in \mathcal{H}} \mathbf{1}_{\{\mathcal{T}_h(Z) \geq \mathcal{T}_{h_0}(Z)\}}.$$

When the total number of labelings $|\mathcal{H}| = \binom{N_1 + N_2}{N_1}$ is too large for exhaustive enumeration, we approximate the exact permutation distribution by Monte Carlo.

Definition 10 (Monte Carlo Permutation p -Value) Let $n \in \mathbb{N}$, $n \geq 1$, denote the number of random permutations (i.e., labelings) to be drawn from \mathcal{H} . Take i.i.d. random variables $H^{(j)} \sim \text{Unif}(\mathcal{H})$ ($1 \leq j \leq n$) independent of Z . A Monte Carlo permutation p -value obtained via Monte Carlo approximation, with standard “+1 correction” (to avoid zero p -values), is given by

$$\hat{p}_n(Z) := \frac{1 + \sum_{j=1}^n \mathbf{1}_{\{T_{H^{(j)}}(Z) \geq \mathcal{T}_{h_0}(Z)\}}}{n + 1} \quad (\text{D1})$$

The following proposition shows that, under the null hypothesis, the permutation test is conservative: both the exact and the Monte Carlo permutation p -values control the Type I error at level α .

Proposition 15 (Conservativeness of Permutation p -Values) *Assume the null hypothesis $H_{\text{null}} : P_1 = P_2$, so that the concatenated sample $Z = \text{concat}(X^{(1)}, X^{(2)})$ is exchangeable with respect to the set of labelings \mathcal{H} . Let T be the test statistic, and let $\mathcal{T}_h(Z) = T(Z_h, Z_{h^c})$ denote its value under labeling $h \in \mathcal{H}$. Let $p_{\text{exact}}(Z)$ and $\hat{p}_n(Z)$ be the exact and Monte Carlo permutation p -values, respectively, defined in the preceding paragraphs. Then, for any $\alpha \in (0, 1)$,*

$$\mathbb{P}(p_{\text{exact}}(Z) \leq \alpha) \leq \alpha.$$

Moreover, there exists an augmented probability space $(\hat{\Omega}, \hat{\mathcal{F}}, \hat{\mathbb{P}})$ carrying i.i.d. random labelings $H^{(1)}, \dots, H^{(n)} \sim \text{Unif}(\mathcal{H})$, independent of Z , such that for every $n \in \mathbb{N}$,

$$\hat{\mathbb{P}}(\hat{p}_n(Z) \leq \alpha) \leq \alpha.$$

Thus both the exact and the Monte Carlo permutation tests are conservative: their Type I error rate does not exceed the nominal level α .

Proof sketch The results are standard properties of permutation tests under the null hypothesis of exchangeability. For any measurable test statistic T , the permutation p -value is known to be super-uniform, that is, $\Pr(p_{\text{exact}} \leq \alpha) \leq \alpha$, and the same holds for its Monte Carlo approximation. A concise treatment can be found in [Lehmann and Romano \(2005\)](#) (Chapter 15) and [Phipson and Smyth \(2010\)](#). \square

To assess the adequacy of the number n of random labelings, we record a bound on the Monte Carlo variability of the permutation p -value.

Proposition 16 (Monte Carlo Variance Bound) *Under the setting described above, we have*

$$\hat{\mathbb{V}}(\hat{p}_n(Z) | Z) \leq \frac{1}{4(n+1)} \quad \text{a.s.},$$

where $\hat{\mathbb{V}}(\cdot | Z)$ denotes the conditional variance under $\hat{\mathbb{P}}$ given Z .

Proof Define

$$p(Z) := \hat{\mathbb{P}}(T_{H^{(j)}}(Z) \geq \mathcal{T}_{h_0}(Z) | Z),$$

which does not depend on j . Conditional on Z , the indicators $I_j(Z) = \mathbf{1}_{\{T_{H^{(j)}}(Z) \geq \mathcal{T}_{h_0}(Z)\}}$ are i.i.d. Bernoulli($p(Z)$), so that $\sum_{j=1}^n I_j(Z) \sim \text{Binomial}(n, p(Z))$. Therefore,

$$\hat{\mathbb{V}}[\hat{p}_n(Z) | Z] = \frac{n p(Z)(1 - p(Z))}{(n+1)^2} \leq \frac{1}{4(n+1)}.$$

\square

Remark 18 (Multiple Testing Across Consecutive Windows) In practical applications, it is often of interest to test whether a sequence of consecutive windows $\mathcal{W}_1, \dots, \mathcal{W}_K$ share a common distribution. This involves testing the series of local null hypotheses

$$H_{\text{null},k} : P_k = P_{k+1}, \quad k = 1, \dots, K-1,$$

simultaneously at a given significance level α . When each test is conducted at level α , the overall probability of at least one false rejection, known as the *family-wise error rate* (FWER), tends to exceed α , making the overall testing procedure *anti-conservative* (i.e., prone to false positives).

A simple and widely used approach to control the FWER is the *Bonferroni correction*, which replaces the nominal level α by $\alpha/(K-1)$ for each of the $K-1$ individual tests. Although the Bonferroni method guarantees that the FWER does not exceed α , it can be overly conservative and thus reduce statistical power.

To improve power while maintaining FWER control, the *Holm step-down procedure* can be applied. Let $p_{(1)} \leq \dots \leq p_{(K-1)}$ be the ordered sequence of individual p -values. Starting from the smallest one, the procedure sequentially rejects $H_{\text{null},(1)}, H_{\text{null},(2)}, \dots$ as long as $p_{(k)} \leq \alpha/(K-k)$ holds, and stops at the first violation of this inequality. All previously rejected hypotheses are then declared significant. This step-down method guarantees FWER control at level α and typically yields higher power than Bonferroni's rule.

An alternative strategy is to replace the local hypotheses above by a single *global null hypothesis*,

$$H_{\text{null}}^{\text{global}} : P_1 = P_2 = \cdots = P_K,$$

and perform a *max-T* test. In this approach, permutation resampling is carried out over the pooled sample $\mathcal{W}_1 \cup \cdots \cup \mathcal{W}_K$, redistributing the data across windows while keeping their sizes fixed. Because the test statistic must be computed for all window pairs under many permutations, the computational cost increases substantially, especially when persistence diagrams are involved.

From a practical viewpoint, when the goal is to promptly detect distributional changes over time, the Bonferroni and Holm step-down procedures often provide a good balance between statistical validity and computational efficiency.

References

Adams H, Emerson T, Kirby M, et al (2017) Persistence images: A stable vector representation of persistent homology. *J Mach Learn Res* 18:1–35

Bubenik P (2015) Statistical topological data analysis using persistence landscapes. *J Mach Learn Res* 16(1):77–102

Carlsson G (2009) Topology and data. *Bull Am Math Soc* 46(2):255–308. <https://doi.org/https://doi.org/10.1090/S0273-0979-09-01249-X>

Carrière M, Chazal F, Glisse M, et al (2021) Optimizing persistent homology based functions. *J Mach Learn Res* 22(272):1–55

Chazal F, Fasy BT, Lecci F, et al (2015) Stochastic convergence of persistence landscapes and silhouettes. *J Comput Geom* 6(2):140–161. <https://doi.org/https://doi.org/10.20382/jocg.v6i2a8>

Cohen-Steiner D, Edelsbrunner H, Harer J (2007) Stability of persistence diagrams. *Discrete Comput Geom* 37(1):103–120

Dłotko P, Helmer N, Stettner L, et al (2024) Topology-driven goodness-of-fit tests in arbitrary dimensions. *Stat Comput* 34:34

Edelsbrunner H, Harer J (2010) Computational Topology: An Introduction. Graduate Studies in Mathematics, American Mathematical Society, Providence, RI

Edelsbrunner H, Letscher D, Zomorodian A (2002) Topological persistence and simplification. *Discrete Comput Geom* 28(4):511–533

Ghrist R (2008) Barcodes: The persistent homology of data. *Bull Am Math Soc* 45(1):61–75. <https://doi.org/https://doi.org/10.1090/S0273-0979-07-01191-3>

Gidea M, Katz Y (2018) Topological data analysis of financial time series: Landscapes of crashes. *Physica A* 491:820–834

Islambekov U, Yuvaraj M, Gel YR (2019) Harnessing the power of topological data analysis to detect change points. *Environ Model Softw* 119:249–258

Lehmann EL, Romano JP (2005) Testing Statistical Hypotheses, 3rd edn. Springer Texts in Statistics, Springer, New York

Li J, Barron AR (2000) Mixture density estimation. *Adv Neural Inf Process Syst* 12:279–285

Lum PY, Singh G, Lehman A, et al (2013) Extracting insights from the shape of complex data using topology. *Sci Rep* 3:1236

McLachlan G, Peel D (2000) Finite Mixture Models. Wiley Series in Probability and Statistics, Wiley, New York

Muirhead RJ (1982) Aspects of Multivariate Statistical Theory. Wiley Series in Probability and Statistics, Wiley, New York

Phipson B, Smyth GK (2010) Permutation p -values should never be zero: Calculating exact p -values when permutations are randomly drawn. *Stat Appl Genet Mol Biol* 9(1):Article 39

Vershynin R (2018) High-Dimensional Probability: An Introduction with Applications in Data Science. Cambridge Series in Statistical and Probabilistic Mathematics, Cambridge Univ. Press, Cambridge

Yao J, Li J, Wu J, et al (2025) Change points detection in financial markets using topological data analysis. SSRN Electron J Available at SSRN: <https://ssrn.com/abstract=5196633>